

1 **A list of all relevant changes**

2

3 Dear editor:

4 Thanks for your work and the referees' contributions to the improvement of our paper. We are very
5 grateful for that. I write to give you a general picture of the major revisions we have made as the
6 referees suggested.

7 (1) We added a quantitative analysis of the effect of aerosols and albedo on differences between
8 retrieved and models XCO₂ as well as differences in retrieved XCO₂ between different algorithms as
9 the two referees suggested.

10 (2) We removed EMMA, one of the algorithms, from the analysis in this paper as the two referees
11 suggested. And we also revised the related analysis results.

12 (3) We shortened the part about ACOS V7.3 and move part of it to the appendix.

13 (4) According to the referees' suggestions, we revised our conclusion and analysis results in Table 7
14 so as to be more concise and conclusive.

15 (5) We corrected improper English in the paper.

16

17 Best regards,

18 Nian

19 Responses to referee #1

20 Responses to Anonymous Referee #1 on the manuscript of “Regional uncertainty of GOSAT XCO₂ retrievals in China:
21 Quantification and attribution”

22

23 Thank you for your suggestions and valuable comments very much. We have fully considered all your comments, and
24 carried out our revision and improved our manuscript accordingly. The item-by-item response to the specific comments is as
25 follows (referee’s comments in **red** and our response in **black**).

26

27 **Referee #1: general:**

28 **-The paper is interesting to the CO₂ remote sensing community although in the end it stays rather inconclusive. The**
29 **reason is that there is no absolute reference for the true XCO₂ in this study. The conclusions that are being drawn**
30 **are based on (in-) consistency between different retrieval algorithms and comparison to the GEOS-CHEM model and**
31 **are hence to large extend speculative.**

32 For inconclusive problem as you point out, we revised our analysis results concluded in Table 7. In this study, we aim
33 to reveal regional uncertainty of GOSAT XCO₂ retrievals via comparison and evaluation of consistence of multi-algorithms
34 for GOSAT observations, and probe the reason why performances of XCO₂ from multi- algorithms are different in same
35 regions. Our results are expected to give a reliable and valuable reference for application of XCO₂ data in detection of
36 carbon source and sink at a regional scale, e.g. the result gotten by our analysis, the better consistence of XCO₂ from four
37 algorithms (ACOS, NIES, OCFP, SRFP) in Eastern China with large anthropogenic CO₂ emissions, can promote us to
38 detect the anthropogenic enhancement of CO₂ concentrations using these XCO₂ data with confidence, and the result, the
39 existing problems in deserts likely influenced by albedo and AOD, is expected to get attentions and improvement.

40

41 **Table 1. Summaries of our analyses for uncertainty of XCO₂ retrievals obtained by GOSAT via inter-comparison of multi-**
42 **algorithms above, including characteristics of regional emissions, albedo, aerosol optical depth, and summary of differences**
43 **between algorithms and bias compared to GEOS-Chem.**

Characteristics of regions and summary of algorithms		Cells from 80 °E to 115 °E within 37 °N-42 °N							
Regions		80	85	90	95	100	105	110	115
Left longitude (°E)									
Characteristics of regions	CO ₂ emissions (Tg/year)* ¹	Low emissions (1.2-57.1)				High emissions (515.2- 821.9)			
	Property of aerosol (AOD)* ²	Dust (0.22- 0.53)		Clear (0.10-0.28)			Urban (0.10-0.37))		
	Surface types (albedo)	Sand desert with high brightness (0.20- 0.26)			Gobi and grassland (0.19-0.22)		Cropland and built-up (0.14-0.17)		

	Consistency of algorithms (pairwise mean absolute differences)	Less Consistency (1.0-1.6 ppm)	Good consistency (0.7-1.1 ppm)
Summary of uncertainty	Bias compared to GEOS-Chem (bias range)	Large biases (1.2-3.1 ppm)	lesser biases excluding NIES (0.0-0.5 ppm)
	General performance of algorithms in spatio- temporal patterns of XCO ₂ compared to GEOS-Chem	ACOS presents the lowest bias (-0.1 ± 1.9 ppm); SRFP is next (-0.2 ± 2.2 ppm) NIES presents the greatest -2.0 ± 2.2 ppm)	

44 *¹ represents the total emissions of CO₂ from CHRED in each cell in 2012. *² is the range of averaged seasonal aerosol
45 optical depth over a year.

46

47

48

49 **-The discussion on the aerosol and albedo effect stays qualitative while a more quantitative analysis would be of**
50 **interest here. I suggest to revise the paper to include a more quantitative analysis of the effect of aerosols and albedo**
51 **on differences in retrieved XCO₂ between different algorithms. This analysis should show to what extent the**
52 **differences between algorithms, and between retrieved and models XCO₂, are correlated with AOD and surface**
53 **albedo. When such an analysis is included I recommend publication of the manuscript in AMT.**

54

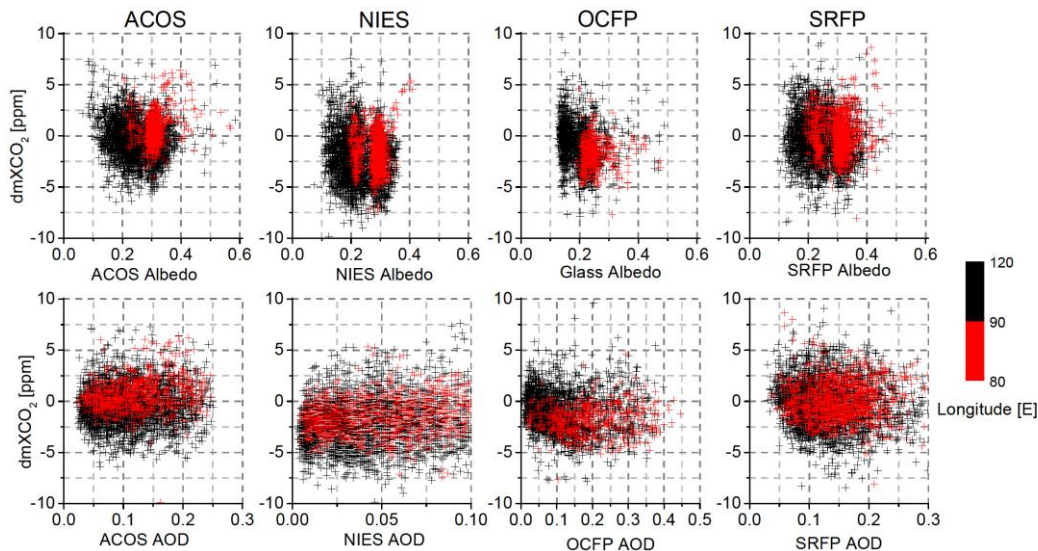
55 According to your suggestion, we added a quantitative analysis about the effect of aerosols and albedo in the discussion
56 section from in the revised manuscript. It is also shown as follows:

57 We discussed the influences of albedo and AOD on XCO₂ retrievals from ACOS, NIES, OCFP and SRFP in further.

58 [Fig. 14](#) plots the scatters of albedo and AOD with the differences between GEOS-XCO₂ data (created in section 3.1) to
59 XCO₂ retrievals, hereafter referred to as dmXCO₂, for ACOS, NIES, OCFP and SRFP. The albedo data obtained from
60 GLASS02B06 is used for OCFP as there are no albedo data available from its released data product.

61 [Fig. 14](#) shows that dmXCO₂ of both ACOS and NIES demonstrate a slightly decreasing trend with albedo whereas
62 slightly increasing trend with AOD. The dmXCO₂ of ACOS tend to be larger in 80 °E -90 °E of deserts with high albedo than
63 that in other regions. The dmXCO₂ of OCFP demonstrate a clear decreasing trend with albedo and AOD comparing to the
64 other algorithms. The dmXCO₂ of SRFP basically does not show a clearly dependence on either albedo or AOD. We further
65 investigated the standard deviation of dmXCO₂ by a variation of the bin-to-bin dmXCO₂ with albedo and AOD. dmXCO₂ is
66 averaged by surface albedo within 0.05 albedo bins and AOD within 0.05 AOD bins, respectively. The standard deviation of
67 the mean dmXCO₂ in each 0.05 albedo (AOD) bins, i.e. a measure of the bin-to-bin dmXCO₂, is calculated. It is found that
68 the dmXCO₂ for the four algorithms change with both albedo and AOD in bin-to-bin. In the whole study area, the standard
69 deviation in albedo is the largest for OCFP, up to 0.7 ppm, while that is smaller from ACOS, NIES and SRFP, 0.4 ppm, 0.3

70 ppm and 0.2 ppm, respectively. The standard deviation of $dmXCO_2$ in AOD is larger for SRFP (0.5 ppm) than those for
 71 ACOS (0.2 ppm), NIES (0.3 ppm) and OCFP (0.4 ppm). Viewing to the deserts (80 E -90 E), the standard deviation in
 72 albedo is the largest from NIES (1.5 ppm), and the smallest from OCFP (0.2 ppm) while they are 1.0 ppm and 0.5 ppm for
 73 ACOS and SRFP, respectively. The standard deviations in AOD, however, are similar (0.2-0.4 ppm) in this area. As a result,
 74 OCFP tend to be more sensitive to albedo and AOD compared to other algorithms. In the deserts, NIES are the most
 75 sensitive XCO_2 retrievals to surface albedo and OCFP the least.

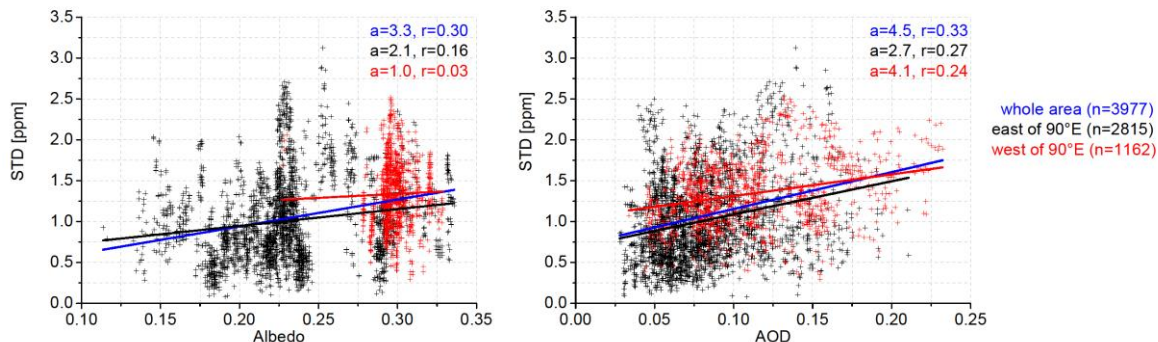


76
 77 **Fig. 1: Scatter plots of the differences ($dmXCO_2$) between GEOS- XCO_2 to ACOS, NIES, OCFP and SRFP respectively, with**
 78 **respect to albedo (the upper panels) and AOD (the lower panels). Colored points represent the data from different cells: red-[80 E,**
 79 **105 E], black-[105 E, 120 E] in the study latitude zone [37 N, 42 N]. Colored solid lines display the corresponding linear**
 80 **regression trend line for the total points. Albedo and AOD are extracted from data products of the retrieval algorithms except**
 81 **albedo data in OCFP in which GLASS data are used.**

82 | Figure [Fig. 15](#), moreover, demonstrates the influence of albedo and AOD on the standard deviation (STD) of XCO_2
 83 from four algorithms at the same footprints (timely in the same day, geometrically located within $\pm 0.01^\circ$ in space).
 84 Averaged albedo (the left panels) and AOD (the right panels) of the four algorithms are used whereas the averaged albedo is
 85 obtained only using three attached albedo in the algorithms except OCFP.

86 | The increasing trends of STD with both albedo and AOD can be seen from [Fig. 15](#). The mean STD is 1.3 ppm in the
 87 western cells (80 E -90 E) where albedo is mostly within 0.25-0.35. This STD is lightly larger than that (1.0ppm) in eastern
 88 cells (90 E-120E) where albedo is comparatively smaller (mostly within 0.15-0.25). It is found from the statistics presented
 89 | in [Fig. 15](#) that the correlation coefficients of STD with albedo and that with AOD is almost the same (both are 0.3) for all the
 90 data. Particular influence from albedo in desert over the western cells can be clearly observed. These results indicate that the

91 inconsistency of XCO₂ retrievals from four algorithms tend to be increase with the enlargements of albedo and AOD so as to
 92 imply that uncertainty of satellite-retrieved XCO₂ should be mostly alerted with the elevations of albedo and AOD.



93
 94 **Fig. 2: Scatter plots of the standard deviation (STD) of XCO₂ from the four algorithms to albedo (the left panel) and AOD (the**
 95 **right panel). Colored points represent different cells: red-[80 E, 105 E], black-[105 E, 120 E] in the latitude zone [37 N, 42 N].**
 96 **Colored solid lines display the corresponding linear regression trend line for the scatter plots with the regression slope (a) and the**
 97 **correlation coefficient (r) also presented. n is the number of samples. Albedo is the mean surface albedo in 0.75-um band from the**
 98 **three algorithms including ACOS, NIES and SRFP. AOD is the mean AOD in 0.75-um band from the four algorithms.**

99

100

101

102 **-Other points:**

103 **--How accurate are the XCO₂ values modeled by GEOS-CHEM? The paper would benefit from a demonstration of**
 104 **the capability of GEOS-CHEM, for example from comparisons with TCCON (albeit outside the study region).**

105 We added comparisons of GEOS-Chem with 14 TCCON sites. The added descriptions and validation results are shown
 106 in the revised manuscript and as follows:

107 We compared GEOS-Chem CO₂ simulations from the global model driven by CHRED with daily mean TCCON data
 108 from 14 TCCON sites (version GGG2014 data version) (Blumenstock et al., 2014; Deutscher et al., 2014; Griffith et al.,
 109 2014a, 2014b; Hase et al., 2014; Kawakami et al., 2014; Kivi et al., 2014; Morino et al., 2014; Sherlock et al., 2014;
 110 Sussmann et al., 2014; Warneke et al., 2014; Wennberg et al., 2014a, 2014b, 2014c). All TCCON measurements between 12
 111 pm and 13:30 pm are used in the comparisons, where GEOS-Chem CO₂ profiles are taken according to the location of
 112 TCCON stations (latitude and longitude) as well as the observing date and transformed to XCO₂ by convolved with the
 113 individual averaging kernel in each station as Wunch (2010) suggested. The statistics results are shown in [Table 5](#).

114 **Table 2. Statistics of comparison between GEOS-Chem CO₂ simulations driven by CHRED and TCCON data from January 2010**
 115 **to February 2013, which includes biases (Δ), the standard deviations (δ), the correlation coefficients (r) and valid days (days) when**
 116 **TCCON data are available. Δ , δ and r are calculated using coincident daily mean data averaged between 12:00 pm and 13:30 pm.**

ID	Station name	Latitude	Longitude	Δ [ppm]	δ [ppm]	r	days
----	--------------	----------	-----------	----------------	----------------	---	------

1	Sodankyla	67.37	26.63	2.03	2.00	0.83	269
2	Bialystok	53.23	23.02	0.49	1.84	0.87	196
3	Karlsruhe	49.1	8.44	0.84	1.69	0.84	152
4	Orleans	47.97	2.11	0.44	1.70	0.85	223
5	Garmisch	47.48	11.06	0.65	1.64	0.83	293
6	Park Falls	45.94	-90.27	1.17	2.14	0.75	494
7	Lamont	36.6	-97.49	-0.04	1.22	0.90	642
8	Tsukuba	36.05	140.12	1.43	1.66	0.75	217
9	JPL	34.2	-118.18	-1.30	1.15	0.90	289
10	Saga	33.24	130.29	-0.39	1.65	0.86	159
11	Izana	28.3	-16.48	0.85	1.04	0.90	114
12	Darwin	-12.43	130.89	0.65	0.90	0.88	447
13	Wollongong	-34.41	150.88	0.53	0.83	0.94	347
14	Lauder	-45.04	169.68	0.92	0.42	0.97	370
Mean				0.59 ± 0.80	1.42 ± 0.50		

117 The results of [Table 5](#) show that the bias ranges from -1.30 to 2.03 ppm for all TCCON sites with standard deviations of
118 the difference varying from 0.42 to 2.14 ppm. The mean standard deviation at the TCCON sites, a measure of the achieved
119 overall precision, from using GEOS-Chem simulations driven by CHRED is 1.42 ± 0.50 ppm which is slightly different
120 from using GEOS-Chem simulations driven by ODIAC (1.41 ± 0.49 ppm). Those validated results with TCCON comparing
121 GEOS-Chem CO₂ simulations driven by CHRED to that by ODIAC indicate that the GEOS-Chem CO₂ simulations driven
122 by CHRED is more likely not to change the global magnitude of CO₂ concentration but rather to depict fine spatial
123 distribution of CO₂ concentration in China.

124
125
126

127 **-- EMMA should be excluded from the analysis in this paper as it is not a retrieval algorithm itself but is composed**
128 **from the different algorithms that are also analyzed in the present study. In fact, each EMMA value is the XCO2**
129 **retrieved by one of the algorithms that is closest to the median value for a given grid box. By including it in this study**
130 **it correlates algorithm to itself.**

131 We removed EMMA from the analysis according to you suggestion and the related analysis were updated in the revised
132 manuscript. Please refer the details to the manuscript. Please refer the details to the revised manuscript because of difficulty
133 in presenting it here since the changes were made across several sections.

134 The new analysis results for four algorithms (ACOS, NIES, OCFP, SRFP) have not changes only Table 5 (new and old
 135 shown as below) have slight changes as EMMA is the median value among multiple algorithms including our discussing
 136 four algorithms.

137 **New Table 5**

138 **The average of the absolute differences (ppm) and standard deviation (ppm) of the target algorithm (in column)**
 139 **matching all other algorithms for each cell. Values in parentheses are the corresponding standard deviations. The**
 140 **differences, which are larger than 1.5 ppm, are highlighted in bold and underlined.**

Left longitude of cells(°E)	80	85	90	95	100	105	110	115
ACOS	1.3(1.1)	1.2(1.0)	1.0(0.7)	1.4(1.2)	1.2(0.9)	1.0(0.7)	0.9(0.6)	0.7(0.5)
NIES	1.1(0.7)	1.3(0.9)	1.2(0.9)	<u>1.6(1.2)</u>	1.1(0.8)	1.1(0.8)	1.1(0.8)	0.9(0.6)
OCFP	<u>1.5(1.1)</u>	1.4(1.0)	1.4(1.0)	1.3(0.9)	1.2(0.9)	0.9(0.6)	0.8(0.6)	0.8(0.6)
SRFP	1.1(0.9)	1.2(1.0)	1.4(1.1)	1.2(0.9)	1.1(0.8)	0.9(0.6)	1.0(0.7)	0.8(0.5)

141 **Old Table 5**

Left longitude of cells(°E)	80	85	90	95	100	105	110	115
ACOS	1.5(0.8)	1.4(0.7)	1.2(0.4)	1.6(1.0)	1.4(0.6)	1.1(0.4)	1.1(0.2)	0.9(0.2)
NIES	1.6(0.2)	1.8(0.4)	1.6(0.4)	<u>2.2(0.6)</u>	1.6(0.3)	1.5(0.3)	1.5(0.3)	1.3(0.2)
OCFP	<u>2.2(0.6)</u>	<u>2.1(0.6)</u>	1.9(0.5)	1.7(0.2)	1.7(0.4)	1.2(0.1)	1.1(0.1)	1.0(0.2)
SRFP	1.3(0.5)	1.4(0.7)	1.6(0.8)	1.4(0.6)	1.3(0.5)	1.1(0.3)	1.2(0.4)	1.0(0.2)
EMMA	1.6(0.9)	1.6(1.0)	1.3(0.6)	1.3(0.6)	1.3(0.6)	1.1(0.5)	1.1(0.4)	1.0(0.4)

142

143 **-- A proper reference should be made to EMMA as a tool to study consistency between different algorithms, like is**
 144 **being done in the present study.**

145 Thanks for this suggestion. We will study the consistency of algorithms for EMMA in further when a proper reference
 146 is available.

147

148 **--Line 132 states: " The recommended bias corrections are applied to the collected XCO2 data from ACOS, OCFP**
 149 **and SRFP". What is meant here? The files for both products already contain bias corrected products. Have these**
 150 **been used?**

151 This is our incorrect expression. Modified to: "The collected XCO2 data from ACOS, OCFP and SRFP are products
 152 after bias correction." .

153

154 **-- Line 364 stated:" while Aerosol Optical Depth (AOD) is greatly affected by high surface albedo because of the**
 155 **optical lengthening effect.". What is meant here? AOD is not affected by surface albedo.**

156 It is our incorrect expression. Modified to: "while estimations of Aerosol Optical Depth (AOD) in GOSAT full physics
 157 CO2 retrieval algorithms are greatly affected by high surface albedo because of atmospheric multiple scattering of light and
 158 the optical lengthening effect" .

159

160 **-- The additional analysis of the new ACOS V7.3 product is confusing. It should either be used in the full analysis or**
 161 **the discussion should be shortened by only stating to what extend the conclusions would be different if the ACOS**
 162 **V7.3 product would have been used. The more detailed analysis could be moved to an appendix.**

163 We shortened the part on the new version of ACOS, and moved part of it to an appendix according to your suggestion.
164 Please refer the details to the revised manuscript. We use ACOS V3.5 instead of ACOS V7.3, the more recently released
165 products, in the analysis because we considered that (1) ACOS V3.5 have been being currently used in our studying group;
166 (2) as described in reference[GES DISC, 2017], which says, *The retrieval algorithm used to create the Build 7 ACOS data*
167 *product is consistent with that used to create the OCO-2 v7.3 data product. This will allow comparison of the ACOS and*
168 *OCO-2 data without having to consider algorithm differences*, ACOS V7.3 are not exactly the newer version of ACOS
169 products.
170

171

172 Responses to referee #2

173 Responses to Anonymous Referee #2 on the manuscript of “Regional uncertainty of GOSAT XCO2 retrievals in China:
174 Quantification and attribution”

175

176 Thank you for your suggestions and valuable comments very much. We have fully considered all your comments, and
177 carried out our revision and improved our manuscript accordingly. The item-by-item response to the specific comments is as
178 follows (referee’s comments in **red** and our response in **black**).

179

180 Referee #2:

181 **Major points : See the comments from the other reviewer :**

182 **- EMMA should be left out as it is the combined product of all other retrieval products shown**

183 We removed EMMA from the analysis according to you suggestion and the related analysis were updated in the revised
184 manuscript. Please refer the details to the revised manuscript because of difficulty in presenting it here since the changes
185 were made across several sections.

186 The new analysis results for four algorithms (ACOS, NIES, OCFP, SRFP) have not changes only Table 5 (new and old
187 shown as below) have slight changes as EMMA is the median value among multiple algorithms including our discussing
188 four algorithms.

189 New Table 5

190 **The average of the absolute differences (ppm) and standard deviation (ppm) of the target algorithm (in column)**
191 **matching all other algorithms for each cell. Values in parentheses are the corresponding standard deviations. The**
192 **differences, which are larger than 1.5 ppm, are highlighted in bold and underlined.**

Left longitude of cells(°E)	80	85	90	95	100	105	110	115
ACOS	1.3(1.1)	1.2(1.0)	1.0(0.7)	1.4(1.2)	1.2(0.9)	1.0(0.7)	0.9(0.6)	0.7(0.5)
NIES	1.1(0.7)	1.3(0.9)	1.2(0.9)	<u>1.6(1.2)</u>	1.1(0.8)	1.1(0.8)	1.1(0.8)	0.9(0.6)
OCFP	<u>1.5(1.1)</u>	1.4(1.0)	1.4(1.0)	1.3(0.9)	1.2(0.9)	0.9(0.6)	0.8(0.6)	0.8(0.6)
SRFP	1.1(0.9)	1.2(1.0)	1.4(1.1)	1.2(0.9)	1.1(0.8)	0.9(0.6)	1.0(0.7)	0.8(0.5)

193 Old Table 5

Left longitude of cells(°E)	80	85	90	95	100	105	110	115
ACOS	1.5(0.8)	1.4(0.7)	1.2(0.4)	1.6(1.0)	1.4(0.6)	1.1(0.4)	1.1(0.2)	0.9(0.2)
NIES	1.6(0.2)	1.8(0.4)	1.6(0.4)	<u>2.2(0.6)</u>	1.6(0.3)	1.5(0.3)	1.5(0.3)	1.3(0.2)
OCFP	<u>2.2(0.6)</u>	<u>2.1(0.6)</u>	1.9(0.5)	1.7(0.2)	1.7(0.4)	1.2(0.1)	1.1(0.1)	1.0(0.2)
SRFP	1.3(0.5)	1.4(0.7)	1.6(0.8)	1.4(0.6)	1.3(0.5)	1.1(0.3)	1.2(0.4)	1.0(0.2)
EMMA	1.6(0.9)	1.6(1.0)	1.3(0.6)	1.3(0.6)	1.3(0.6)	1.1(0.5)	1.1(0.4)	1.0(0.4)

194

195 **- Shorten the part on the new version of ACOS, or use only the new version data**

196 We shortened the part on the new version of ACOS, and moved part of it to the appendix according to your suggestion.
197 Please refer the details to the revised manuscript. We use ACOS V3.5 instead of ACOS V7.3, the more recently released
198 products, in the analysis because we considered that (1) ACOS V3.5 have been being currently used in our studying group;
199 (2) as described in reference[GES DISC, 2017], which says, *The retrieval algorithm used to create the Build 7 ACOS data*
200 *product is consistent with that used to create the OCO-2 v7.3 data product. This will allow comparison of the ACOS and*

201 *OCO-2 data without having to consider algorithm differences*, ACOS V7.3 is not exactly the newer version of ACOS
202 products.

203

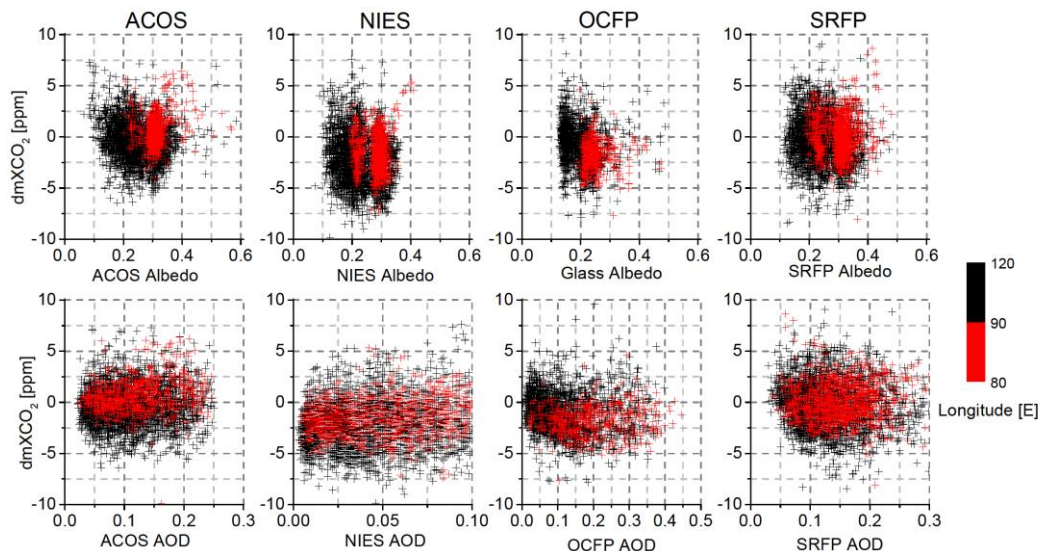
204 **- Provide a more quantitative analysis of the effect of aerosols and albedo on the observed differences between**
205 **different algorithms**

206 According to your suggestion, we added a quantitative analysis about the effect of aerosols and albedo in the discussion
207 section in the revised manuscript and presented it here:

208 We discussed the influences of albedo and AOD on XCO₂ retrievals from ACOS, NIES, OCFP and SRFP in further.

209 [Fig. 14](#) plots the scatters of albedo and AOD with the differences between GEOS-XCO₂ data (created in section 3.1) to
210 XCO₂ retrievals, hereafter referred to as dmXCO₂, for ACOS, NIES, OCFP and SRFP. The albedo data obtained from
211 GLASS02B06 is used for OCFP as there are no albedo data available from its released data product.

212 [Fig. 14](#) shows that dmXCO₂ of both ACOS and NIES demonstrate a slightly decreasing trend with albedo whereas
213 slightly increasing trend with AOD. The dmXCO₂ of ACOS tend to be larger in 80 °E -90 °E of deserts with high albedo than
214 that in other regions. The dmXCO₂ of OCFP demonstrate a clear decreasing trend with albedo and AOD comparing to the
215 other algorithms. The dmXCO₂ of SRFP basically does not show a clearly dependence on either albedo or AOD. We further
216 investigated the standard deviation of dmXCO₂ by a variation of the bin-to-bin dmXCO₂ with albedo and AOD. dmXCO₂ is
217 averaged by surface albedo within 0.05 albedo bins and AOD within 0.05 AOD bins, respectively. The standard deviation of
218 the mean dmXCO₂ in each 0.05 albedo (AOD) bins, i.e. a measure of the bin-to-bin dmXCO₂, is calculated. It is found that
219 the dmXCO₂ for the four algorithms change with both albedo and AOD in bin-to-bin. In the whole study area, the standard
220 deviation in albedo is the largest for OCFP, up to 0.7 ppm, while that is smaller from ACOS, NIES and SRFP, 0.4 ppm, 0.3
221 ppm and 0.2 ppm, respectively. The standard deviation of dmXCO₂ in AOD is larger for SRFP (0.5 ppm) than those for
222 ACOS (0.2 ppm), NIES (0.3 ppm) and OCFP (0.4 ppm). Viewing to the deserts (80 °E -90 °E), the standard deviation in
223 albedo is the largest from NIES (1.5 ppm), and the smallest from OCFP (0.2 ppm) while they are 1.0 ppm and 0.5 ppm for
224 ACOS and SRFP, respectively. The standard deviations in AOD, however, are similar (0.2-0.4 ppm) in this area. As a result,
225 OCFP tend to be more sensitive to albedo and AOD compared to other algorithms. In the deserts, NIES are the most
226 sensitive XCO₂ retrievals to surface albedo and OCFP the least.

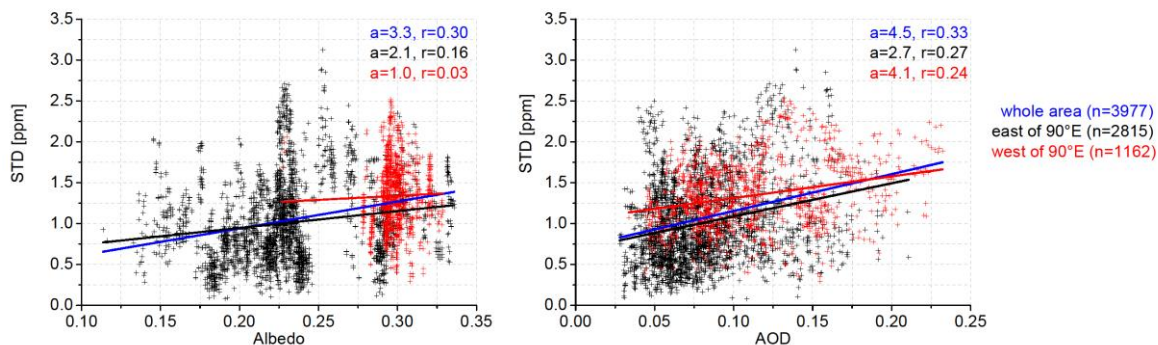


227

228 **Fig. 3: Scatter plots of the differences ($dmXCO_2$) between GEOS- XCO_2 to ACOS, NIES, OCFP and SRFP respectively, with**
 229 **respect to albedo (the upper panels) and AOD (the lower panels). Colored points represent the data from different cells: red-[80 E,**
 230 **105 E], black-[105 E, 120 E] in the study latitude zone [37 N, 42 N]. Colored solid lines display the corresponding linear**
 231 **regression trend line for the total points. Albedo and AOD are extracted from data products of the retrieval algorithms except**
 232 **albedo data in OCFP in which GLASS data are used.**

233 | Figure [Fig. 15](#), moreover, demonstrates the influence of albedo and AOD on the standard deviation (STD) of XCO_2
 234 from four algorithms at the same footprints (timely in the same day, geometrically located within $\pm 0.01^\circ$ in space).
 235 Averaged albedo (the left panels) and AOD (the right panels) of the four algorithms are used whereas the averaged albedo is
 236 obtained only using three attached albedo in the algorithms except OCFP.

237 | The increasing trends of STD with both albedo and AOD can be seen from [Fig. 15](#). The mean STD is 1.3 ppm in the
 238 western cells (80°E -90°E) where albedo is mostly within 0.25-0.35. This STD is lightly larger than that (1.0ppm) in eastern
 239 cells (90°E-120E°) where albedo is comparatively smaller (mostly within 0.15-0.25). It is found from the statistics presented
 240 | in [Fig. 15](#) that the correlation coefficients of STD with albedo and that with AOD is almost the same (both are 0.3) for all the
 241 data. Particular influence from albedo in desert over the western cells can be clearly observed. These results indicate that the
 242 inconsistency of XCO_2 retrievals from four algorithms tend to be increase with the enlargements of albedo and AOD so as to
 243 imply that uncertainty of satellite-retrieved XCO_2 should be mostly alerted with the elevations of albedo and AOD.



244

245 **Fig. 4: Scatter plots of the standard deviation (STD) of XCO₂ from the four algorithms to albedo (the left panel) and AOD (the**
 246 **right panel). Colored points represent different cells: red-[80 °E, 105 °E], black-[105 °E, 120 °E] in the latitude zone [37 °N, 42 °N].**
 247 **Colored solid lines display the corresponding linear regression trend line for the scatter plots with the regression slope (a) and the**
 248 **correlation coefficient (r) also presented. n is the number of samples. Albedo is the mean surface albedo in 0.75-um band from the**
 249 **three algorithms including ACOS, NIES and SRFP. AOD is the mean AOD in 0.75-um band from the four algorithms.**

250

251

252

253 **- Provide some clear evidence of performance of GEOS-Chem wrt total column XCO₂**

254 We added comparisons of GEOS-Chem with 14 TCCON sites. The added descriptions and validation results are shown
 255 in the revised manuscript and as follows:

256 We compared GEOS-Chem CO₂ simulations from the global model driven by CHRED with daily mean TCCON data
 257 from 14 TCCON sites (version GGG2014 data version) (Blumenstock et al., 2014; Deutscher et al., 2014; Griffith et al.,
 258 2014a, 2014b; Hase et al., 2014; Kawakami et al., 2014; Kivi et al., 2014; Morino et al., 2014; Sherlock et al., 2014;
 259 Sussmann et al., 2014; Warneke et al., 2014; Wennberg et al., 2014a, 2014b, 2014c). All TCCON measurements between 12
 260 pm and 13:30 pm are used in the comparisons, where GEOS-Chem CO₂ profiles are taken according to the location of
 261 TCCON stations (latitude and longitude) as well as the observing date and transformed to XCO₂ by convolved with the
 262 individual averaging kernel in each station as Wunch (2010) suggested. The statistics results are shown in [Table 5](#).

263 **Table 3. Statistics of comparison between GEOS-Chem CO₂ simulations driven by CHRED and TCCON data from January 2010**
 264 **to February 2013, which includes biases (Δ), the standard deviations (δ), the correlation coefficients (r) and valid days (days) when**
 265 **TCCON data are available. Δ , δ and r are calculated using coincident daily mean data averaged between 12:00 pm and 13:30 pm.**

ID	Station name	Latitude	Longitude	Δ [ppm]	δ [ppm]	r	days
1	Sodankyla	67.37	26.63	2.03	2.00	0.83	269
2	Bialystok	53.23	23.02	0.49	1.84	0.87	196
3	Karlsruhe	49.1	8.44	0.84	1.69	0.84	152
4	Orleans	47.97	2.11	0.44	1.70	0.85	223
5	Garmisch	47.48	11.06	0.65	1.64	0.83	293
6	Park Falls	45.94	-90.27	1.17	2.14	0.75	494
7	Lamont	36.6	-97.49	-0.04	1.22	0.90	642
8	Tsukuba	36.05	140.12	1.43	1.66	0.75	217

9	JPL	34.2	-118.18	-1.30	1.15	0.90	289
10	Saga	33.24	130.29	-0.39	1.65	0.86	159
11	Izana	28.3	-16.48	0.85	1.04	0.90	114
12	Darwin	-12.43	130.89	0.65	0.90	0.88	447
13	Wollongong	-34.41	150.88	0.53	0.83	0.94	347
14	Lauder	-45.04	169.68	0.92	0.42	0.97	370
Mean				0.59 ± 0.80	1.42 ± 0.50		

266 The results of [Table 5](#) show that the bias ranges from -1.30 to 2.03 ppm for all TCCON sites with standard deviations of
267 the difference varying from 0.42 to 2.14 ppm. The mean standard deviation at the TCCON sites, a measure of the achieved
268 overall precision, from using GEOS-Chem simulations driven by CHRED is 1.42 ± 0.50 ppm which is slightly different
269 from using GEOS-Chem simulations driven by ODIAC (1.41 ± 0.49 ppm). Those validated results with TCCON comparing
270 GEOS-Chem CO₂ simulations driven by CHRED to that by ODIAC indicate that the GEOS-Chem CO₂ simulations driven
271 by CHRED is more likely not to change the global magnitude of CO₂ concentration but rather to depict fine spatial
272 distribution of CO₂ concentration in China.

273
274
275

276 **Minor : Textual suggestions :**

277

278 **-p.2 line 46 : I think you should leave out TanSat in that particular sentence as that instrument has not yet**
279 **contributed to a better understanding of...as far as I know.**

280 Yes, TanSat have not produces XCO2 data available as to its some problems as you know. We removed the description
281 of TanSat in the revised manuscript.

282

283 **-p.3 line 85-86 : rephrase 'that trend ...to east' because unclear what is meant**

284 Modified to: " there are anthropogenic emissions increasing from west to east." in line 83.

285

286 **-p.9 GLASS albedo is used. For which wavelength is this albedo?**

287 It is broadband albedo product rather than albedo in narrow bands. The following was added: " GLASS02B06 is a daily
288 land-surface shortwave (300-3000nm) broadband albedo product in temporal resolution of eight days.".

289

290 **-table 2. Add to the table caption : All biases > 1 ppm are underlined.**

291 We added it in the caption of table 3, which is the previous table 2. The caption is modified to: "The biases (ppm) and
292 their standard deviations (ppm) of the four algorithms vs GEOS-Chem in each cell, where the upper line indicates bias (the
293 corresponding standard deviations in parenthesis) for each algorithm vs GEOS-Chem and the lower line is the available
294 number of used samples. The biases, larger than 1 ppm, are highlighted in bold and underlined." in the revised manuscript.

295

296 **-Change 'the values in parentheses are the biases and their ...' → 'the values are the biases and -in parentheses-**
297 **their...'**

298 We revised this incorrect description, which also refers to the caption of table 3, in the revised manuscript. If you have
299 read the last item, the following five lines can be skipped.

300 The caption is modified to:“The biases (ppm) and standard deviation (ppm) of the four algorithms vs GEOS-Chem in
301 each cell, where the upper line indicates bias(the standard deviations) for each algorithm vs GEOS-Chem and the lower line
302 is the number of used samples. The biases, larger than 1 ppm, are highlighted in bold and underlined.” in the revised
303 manuscript.

304

305 **-Table 3 table caption. What are the underlined values ?**

306 They are differences (ppm) larger than 1.5 ppm between two algorithms (column algorithm minus row algorithm) for
307 each cell.

308 The caption of Table 4, which is the previous table 3, was modified to: “Differences (ppm) between two algorithms
309 (column algorithm minus row algorithm) and the standard deviation (ppm) for each cell, where values in parentheses are the
310 corresponding standard deviations. The differences, larger than 1.5 ppm, are highlighted in bold and underlined.” in the
311 revised manuscript.

312

313 **p.18 line 350 ('To summarize the quantification...SRFP') : I do not understand this sentence given the data.**

314 Thank you for pointing it out. This sentence has been deleted in the revised manuscript because we are also aware that
315 this sentence makes the results confusing.

316

317 **-Fig. 8 Figure caption 'and the differences of detrended.... and GEOS-Chem' should that be '... with GOES-Chem' ?**

318 Corrected. Modified to :” The spatial (in the study latitude band) and temporal (in seasons) changing patterns of
319 detrended XCO₂ from ACOS, NIES, OCFP, SRFP retrievals and GEOS-Chem simulations (left) and the differences of
320 detrended XCO₂ to GEOS-Chem for ACOS, NIES, OCFP and SRFP.”

321

322 **-p.21 line 423/424 I do not understand the sentence 'No bias was found ...R2=0.77' based on what I see in Table 6.**
323 **Also it is not consistent with what is written in line429/430.**

324 It is our incorrect expression. The results that no bias was found in ACOS V7.3 from GEOS-Chem with a standard
325 deviation of 1.6 ppm and R2=0.77, is for the whole study area. The original Line 429/430 which states, “*It can also be found*
326 *from Table 6 that the bias of ACOS V7.3 relative to GEOS-Chem is within 0.3 ppm but above 1.3 ppm, in cells east and west*
327 *of 90°E, respectively.*”, is focused on the regional performance.

328 The sentence has been modified to:” No bias was found in ACOS V7.3 from GEOS-Chem with a standard deviation of
329 1.6 ppm and R2 of 0.77 in the whole study area.” in the appendix.

330

331 **-p. 23, line 462 results above → results described above**

332 Corrected.

333

334 **Marked-up manuscript version**

335

336 **Regional uncertainty of GOSAT XCO₂ retrievals in China:**
337 **Quantification and attribution**

338

339 Nian Bie^{1, 2}, Liping Lei¹, ZhaoCheng Zeng³, Bofeng Cai⁴, Shaoyuan Yang^{1, 2}, Zhonghua He^{1, 2},
340 Changjiang Wu^{1, 2}, and Ray Nassar⁵

341 ¹Key Laboratory of Digital Earth Science, Institute of Remote Sensing and Digital Earth, Chinese Academy of Sciences,
342 Beijing 100094, China

343 ²University of Chinese Academy of Sciences, Beijing 100049, China

344 ³Division of Geological and Planetary Sciences, California Institute of Technology, Pasadena, CA91125, USA

345 ⁴The Center for Climate Change and Environmental Policy, Chinese Academy for Environmental Planning, Ministry of
346 Environmental Protection, Beijing, 100012, China

347 ⁵Climate Research Division, Environment and Climate Change Canada, Canada

348 *Correspondence to:* leilp@radi.ac.cn

349 **Abstract.** The regional uncertainty of XCO₂ (column-averaged dry air mole fraction of CO₂) retrieved using different
350 algorithms from the Greenhouse gases Observing SATellite (GOSAT) and its attribution are still not well understood. This
351 paper investigates the regional performance of XCO₂ within a latitude band of 37°N~ 42°N segmented into 8 cells in a grid
352 of 5 ° from west to east (80°E ~120°E) in China, where there are typical land surface types and geographic conditions. The
353 former include the various land covers of desert, grassland and built-up areas mixed with cropland, and the latter include
354 anthropogenic emissions that change from small to large from west to east, including those from the megacity of Beijing. For
355 these specific cells, we evaluate the regional uncertainty of GOSAT XCO₂ retrievals by quantifying and attributing the
356 consistency of XCO₂ retrievals from four algorithms (ACOS, NIES, OCFP, and SRFP) by intercomparison. Particularly,
357 these retrievals are compared with simulated XCO₂ by the high-resolution nested model in East Asia of Goddard Earth
358 Observing System 3-D chemical transport model (GEOS-Chem). We introduce the anthropogenic CO₂ emissions data
359 generated from the investigation of surface emitting point sources that was conducted by the Ministry of Environmental
360 Protection of China to GEOS-Chem simulations of XCO₂ over the Chinese mainland. The results indicate that (1) regionally,
361 the four algorithms demonstrate smaller absolute biases of 0.7-1.1 ppm in eastern cells, which are covered by built-up areas
362 mixed with cropland with intensive anthropogenic emissions, than those in the western desert cells (1.0-1.6 ppm) with a
363 high-brightness surface from the pairwise comparison results of XCO₂ retrievals. The inconsistency of XCO₂ from the four
364 algorithms tends to be high in the Taklimakan Desert in western cells, which is likely induced by high surface albedo in
365 addition to dust aerosols in this region. (2) Compared with XCO₂ simulated by GEOS-Chem (GEOS-XCO₂), the XCO₂
366 values of ACOS and SRFP have better agreement with GEOS-XCO₂, while OCFP is the least consistent with GEOS-XCO₂.

367 (3) Viewing attributions of XCO₂ in the spatio-temporal pattern, ACOS and SRFP demonstrate similar patterns, while OCFP
368 is largely different from the others. In conclusion, the discrepancy in the four algorithms is the smallest in eastern cells in the
369 study area, where the megacity of Beijing is located and where there are strong anthropogenic CO₂ emissions, which implies
370 that XCO₂ from satellite observations could be reliably applied in the assessment of atmospheric CO₂ enhancements induced
371 by anthropogenic CO₂ emissions. The large inconsistency among the four algorithms presented in western deserts with a
372 high albedo and dust aerosols, moreover, demonstrates that further improvement is still necessary in such regions, even
373 though many algorithms have endeavored to minimize the effects of aerosols scattering and surface albedo.
374
375 Key words: GOSAT, XCO₂ retrieval algorithms, simulated XCO₂ by GEOS-Chem, regional uncertainty, anthropogenic
376 emissions, and desert

377 **1 Introduction**

378 The column-averaged dry air mole fraction of CO₂ (XCO₂) derived from satellite observations, such as the SCanning
379 Imaging Absorption spectroMeter of Atmospheric CHartographY (SCIAMACHY) (Burrows et al., 1995; Bovensmann et al.,
380 1999), the Greenhouse gases Observing SATellite (GOSAT) (Yokoda et al., 2004), Orbiting Carbon Observatory (OCO-2)
381 (Crisp et al., 2004), ~~and Chinese Carbon Satellite (TanSat) (Liu et al., 2013)~~, have greatly improved our understanding of the
382 variation in atmospheric CO₂ concentration and carbon sources and sinks at a global and regional scale. There have been
383 several full-physics retrieval algorithms specially developed for retrieving XCO₂ from the GOSAT observed spectrum,
384 mainly including the NASA Atmospheric CO₂ Observations from Space (ACOS) (O'Dell et al., 2012), the National Institute
385 for Environmental Studies (NIES) (Yoshida et al., 2013), the University of Leicester full-physics XCO₂ (OCFP) (Cogan et
386 al., 2012) and the RemoTeC XCO₂ Full Physics (SRFP) (Butz et al., 2011).

387 Retrieval of XCO₂ from space is susceptible to the effects of light path changes due to aerosol scattering, uncertainties
388 in observed spectrum and surface states (O'Dell et al., 2012; Oshchepkov et al., 2013). The bias and performance of XCO₂
389 retrievals from an algorithm could change in different regions with differing land surfaces and anthropogenic emissions.
390 Spatio-pattern attributions of XCO₂ viewed from different algorithms are also different, even in the same region, due to
391 different physical approaches adopted by the algorithms, assumptions of atmospheric conditions (aerosol, surface pressure,
392 CO₂ profile, etc.), and pre- and post-processing filters. Currently, the validation of XCO₂ retrievals from different algorithms
393 focuses on using ground-based measurements from Total Carbon Column Observing Network (TCCON) sites (Wunch et al.,
394 2011; Yoshida et al., 2013; Hewson, 2016; Buchwitz et al., 2015, Detmers et al., 2015, Oshchepkov et al., 2013) and their
395 consistency evaluation and cross-comparison both at a global scale and in continental regions (Kulawik et al., 2016;
396 Lindqvist et al., 2015; Lei et al., 2014). The precision and uncertainty of satellite-retrieved XCO₂ outside TCCON stations,
397 most of which are located remote from regions with abundant biosphere fluxes and human activities, are still not well
398 evaluated. The sparseness of TCCON stations over the globe, moreover, means a lack of enough ground observations to

399 validate satellite retrievals. Specifically, there are no good TCCON data available in China, and only a few satellite retrievals
400 have been validated using ground-based Fourier Transform Spectrometer (FTS) XCO₂ measurements in Hefei (Wang et al.,
401 2017). In the analysis and application of XCO₂ data from ACOS, NIES, OCFP and SRFP, we found that unreasonably high
402 XCO₂ was presented in the Taklimakan desert in China (Bie et al., 2016; Liu et al., 2015). For this reason, we extended the
403 study scope to select a longer study period and to further assess the overall performance of these four algorithms at a
404 regional scale.

405 With the advantage of continuity in space and time, atmospheric transport model simulation of CO₂ has been widely
406 used in assessing the performance of satellite-retrieved XCO₂ (Cogan et al., 2012; Lindqvist et al., 2015; Kulawik et al.,
407 2016). As anthropogenic emission of CO₂ is the major contributor to increases of CO₂ in the atmosphere, many studies have
408 been involved in deriving estimates of anthropogenic CO₂ emissions (Oda et al., 2011; Andres et al., 2011). It is known that
409 there exists high uncertainty in estimates of CO₂ emissions from both the burning of fossil fuel and cement production (FF
410 CO₂ emissions) throughout China (Guan et al., 2012; Liu et al., 2015). As noted by Andrews et al. (2012), there exist many
411 kinds of restrictions (e.g., commercial competitiveness reasons) in obtaining accurate data on sub-national (e.g., large-point-
412 source or provincial) FF CO₂ emissions. Furthermore, the assumption of uniform per-capita emissions within a country has
413 also been shown to be unreliable for large countries with diversified economies and electricity-generation methods (Nassar et
414 al., 2013). In the previous study of Keppel-Aleks (2013), the simulated Chinese XCO₂ data was increased by a national
415 uniform ratio for the corresponding XCO₂ contributed by fossil sources to account for the underestimation in Chinese
416 emissions, in which way the spatial variability of Chinese FF emissions was not considered sufficient.

417 In this paper, we focus on a latitude band of 37°N-42°N from 80°E to 120°E in China, where there are various typical
418 land covers such as desert, including the Taklimakan desert, and grassland and built-up areas mixed with croplands,
419 including the megacity of Beijing, and there are anthropogenic emissions ~~increasing that trend from small amounts to large~~
420 ~~amounts~~ from west to east. In this band, the inconsistencies of XCO₂ values derived from four algorithms including ACOS
421 V3.5, NIES V02.21, OCFP V6.0 and SRFP V2.3.7 are compared and evaluated in this paper. A forward model simulation
422 data set from GEOS-Chem, moreover, is also used for intercomparison. To improve the simulation of CO₂ concentration by
423 GEOS-Chem, we introduced a new emission data set, the Chinese High Resolution Emission Gridded Data (CHRED) which
424 is produced by the Ministry of Environmental Protection, China (MEP) based on investigations of emitting point sources
425 from approximately 150 million enterprises throughout the country in 2012 (Wang et al., 2014; Cai et al., 2014).

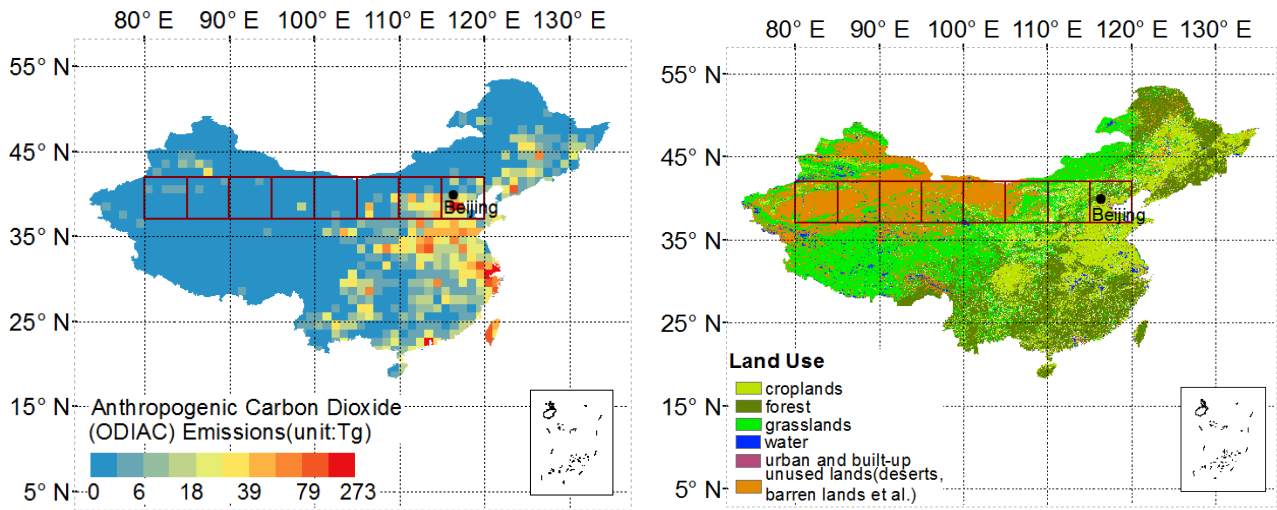
426 First, we aim to reveal the regional uncertainty of XCO₂ observed by GOSAT for the different land covers and
427 anthropogenic CO₂ emission regions by quantifying the inconsistency of the four retrieval algorithms. Second, we aim to
428 provide a reasonable and valuable reference for the analysis and application of XCO₂ data when using these XCO₂ data from
429 the four algorithms. Sec. 2 in this paper describes the XCO₂ retrievals data from four algorithms and the implementation of
430 XCO₂ simulated by GEOS-Chem using CHRED. Inconsistencies of XCO₂ datasets among the four algorithms are quantified
431 and evaluated by (1) pairwise comparisons of XCO₂ between algorithms and (2) comparisons with GEOS-Chem simulations
432 in Sec. 3. The spatio-temporal patterns of XCO₂ from each algorithm are investigated using a combination of sine and cosine

433 trigonometric functions to fit monthly averaged XCO₂ from March 2010 to February 2013 in Sec. 4. Furthermore, the most
434 likely attribution-affecting factors on regional inconsistency, including aerosol and surface albedo, are discussed in Sec. 5.
435 The latest ACOS V7.3 dataset, moreover, is also ~~evaluated~~used by cross-comparisons with GEOS-Chem and other
436 algorithms including ACOS V3.5, NIESV02.21, OCFP V6.0 and SRFP V2.3.7, as shown in subsections of Sec. 5. Finally,
437 the regional performances of four algorithms and the regional uncertainty of GOSAT XCO₂ retrievals from the results
438 described above are summarized, and conclusions are given in Sec. 6.

439 **2 Study area and data**

440 **2.1 Study area**

441 The latitude band of 37°N~42°N from 80°E to 120°E in China is selected as the study area, which is segmented into eight
442 cells in a grid of 5°x5° units for comparison and evaluation. The study area has two typical surface characteristics as shown
443 in Fig. 1, supporting our assessment of the performance of XCO₂ retrievals from four algorithms: (1) the amounts of
444 anthropogenic CO₂ emissions from west to east significantly varies from small to large as shown in Fig. 5(a). The emission
445 data are from the Open-source Data Inventory for Anthropogenic CO₂ (ODIAC), a global annual fossil fuel CO₂ emission
446 inventory developed by combining a worldwide point-source database and satellite observations of the global nightlight
447 distribution (Oda et al., 2011). There are almost no anthropogenic CO₂ emissions in the western cells ending at 105°E, while
448 there is high anthropogenic emission located in the cells on the eastern end of the latitude band. (2) There are typical land
449 covers from west to east, as shown in Fig. 5 (b), mainly composed of desert (desert sand in the two cells from 80°E to 90°E,
450 Gobi in the two cells from 90°E to 100°E, desert sand in the cell of 100°E-105°E), grassland in the cell of 105°E-110°E, and
451 cropland and built-up areas in the two cells from 110°E to 120°E. These characteristics are associated with complicated
452 aerosol compositions and loadings. One of the main reasons for focusing on this latitude band, moreover, is because there are
453 more high-quality GOSAT scans available in this area compared to other areas in China.



454

455 **Fig. 5. (a) Location of the study area segmented into cells (deep red cells) in China and annual fossil fuel CO₂ emission in 2012 (1 x**
 456 **1 degree) from ODIAC and (b) land use mapping in 2010, where the black dot represents Beijing, the capital of China.**

457

458 2.2 GOSAT XCO₂ dataset derived from four algorithms

459 We collected XCO₂ data from March 2010 to February 2013 derived from four algorithms: ACOS V3.5
 460 (<http://CO2.jpl.nasa.gov>), NIES V02.21 (RA version with GU screening scheme) (<https://data2.gosat.nies.go.jp>), OCFP
 461 V6.0 (<http://www.esa-ghg-cci.org>) and SRFP V2.3.7 (<http://www.esa-ghg-cci.org>). AOD and surface albedo in 0.75-um O₂
 462 band, which are necessary for our further analysis, are also collected from attached datasets in each algorithms except that
 463 albedo is not available for OCFP. The major characteristics of the four algorithms and the relevant references are listed in
 464 Table 4. The validation at TCCON sites for all algorithms indicates that the bias is less than 1.2 ppm on average and that the
 465 standard deviation is less than 2.0 ppm. All algorithms take aerosol optical depth (AOD) into consideration in their data
 466 screening scheme but in slightly different ways. ~~The recommended bias corrections are applied to the collected XCO₂ data~~
 467 ~~from ACOS, OCFP and SRFP.~~ The collected XCO₂ data from ACOS, OCFP and SRFP are the products after bias
 468 correction. Data observed with high gain and passing the corresponding recommended quality control criteria are used in
 469 ACOS, NIES, OCFP and SRFP.

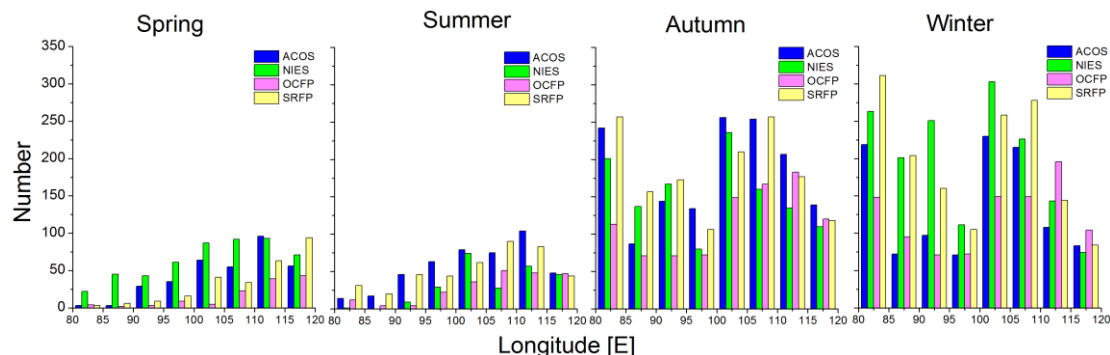
471 **Table 4 Summary of validating results with TCCON, data screening schemes, consideration in scattering and bias corrections for**
 472 **the four retrieval algorithms.**

	ACOS	NIES	OCFP	SRFP
Validation with TCCON ^{*1}	0.3 ppm 1.7 ppm	-1.2 ppm 2.0 ppm	0.04 ppm 1.78 ppm	0.01 ppm 1.93 ppm
Data screening schemes	Aerosol_total_aod: 0.015 to 0.25 Sounding_altitude:<3000 0.55<XCO ₂ _uncer<2.0 ppm Aod_dust<0.15 The difference of the retrieved and priori surface pressure from the A-band cloud-screen $\Delta P_{s,cl d}$: (-12,4.1) hPa	Retrieved aerosol optical thickness: <=0.1 Difference of retrieved and a priori surface pressure: <=20 hpa Blended albedo: <1	Retrieved type 1 (small) AOD: <=0.3 Retrieved type 2 (large) AOD: <=0.15 Retrieved ice type AOD: <=0.025 Error on retrieved XCO ₂ :<=2.15	Aerosol optical thickness : <0.3 3<aero_size<5 0<aerosol_filter<300 Error on retrieved XCO ₂ : <1.2 ppm standard deviation of surface elevation within GOSAT ground pixel: <80 m Blended albedo: <0.9
Consideration in scattering	4 extinction profiles (two aerosol types , water and ice cloud)	logarithms of the mass mixing ratios of fine-mode aerosols and coarse mode aerosols with aerosol optical properties based on SPRINTARS V3.84	Aerosol profile scaling of 2 different aerosol types; cloud extinction profile scaling	Aerosol particle number concentration, aerosol size parameter, aerosol height
Bias corrections	$X'_{CO_2} = X_{CO_2} - 0.5 - 0.155 * (\Delta P_{s,cl d} + 2.7) + 10.6 * (\alpha'_3 - 0.204) + 0.0146 * (\Delta GRAD_{CO_2} - 35) + 12.8 * (AOD_{DUST} - 0.01)$ See details in the product user guide.	-	Via a regression analysis of the difference between GOSAT and TCCON XCO ₂ land observations. See details in the product user guide	$X'_{CO_2} = X_{CO_2} * (1.002837 + 2.1176e - 5 * \phi)$ ϕ : the aerosol filter
References	GES DISC, 2016; O'Dell et al., 2012; D.Wunch et al., 2011.	NIES (GOSAT Project Office), 2015; Yoshida et al., 2013; D.Wunch et al., 2011.	Hew, 2016; GHG-CCI group at University of Leicester, 2014.	Detmers et al., 2015; Hasekamp et al., 2015

473 ^{*1}The first represents mean biases, and the second represents overall standard deviations.

474 Within the study area, the total numbers of valid GOSAT XCO₂ observations are 3345, 3556, 2282 and 3685 for ACOS,
 475 NIES, OCFP and SRFP, respectively. Figure 2 shows the number of available XCO₂ retrievals for 4 seasons (spring: MAM;
 476 summer: JJA; autumn: SON; winter: DJF). It can be seen that the number of available XCO₂ retrievals is clearly smaller in
 477 spring and summer than that in autumn and winter due to different meteorological conditions and data-screening processes.

478 The cloudiness in spring and summer caused by the monsoon climate disturbs satellite observation, while the smaller data
 479 number in the west of 110 °E is due to frequent dust storm in the Taklimakan Desert.



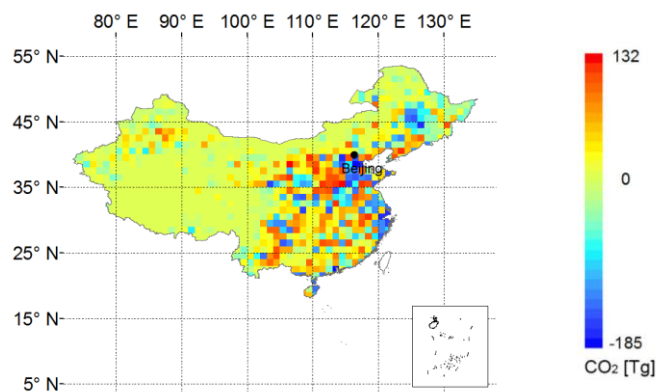
480

481 **Fig. 6. Number of single scans from the four GOSAT-XCO₂ data sets from ACOS, NIES, OCFP and SRFP over each 5x5 ° cells for**
 482 **different seasons (Spring: MAM; summer: JJA; autumn: SON; winter: DJF) from March 2010 to February 2013.**

483 2.3 XCO₂ simulations from GEOS-Chem

484 We use GEOS-Chem version 10-01 driven by GEOS-5 and the details of the main input emissions are as follows: 1) Fossil
 485 fuel fluxes are taken from the new emission data set CHRED for the Chinese mainland, we also use ODIAC version 2013 for
 486 comparison with CHRED. 2) The balanced biosphere CO₂ uptake and emission fluxes are taken from the Simple Biosphere
 487 Model version 3 (SiB3) [Messerschmidt et al. 2012]. 3) Biomass emissions are taken from Global Fire Emission Database
 488 version 4 (GFEDv4) (Giglio et al., 2013). 4) Ocean fluxes are taken as Takahashi et al. (2009) suggested. A detailed
 489 description of these input emissions for the GEOS-Chem CO₂ simulation is presented in Nassar et al. (2010), although we
 490 have used some of the most recent updates available in the GEOS-Chem version 10-01 and the Harvard–NASA Emission
 491 Component version 1.0 (HEMCO) module (Keller et al., 2014), a versatile component for emissions in atmospheric models.
 492 Higher model resolution is critical in the calculation of the concentrations of atmospheric gases, especially over land where
 493 topography smoothing (compared to reality) is determined by horizontal resolution (Ciais et al., 2010). Considering this,
 494 GEOS-Chem nested grid model in China at 0.5 ° (latitude) x 0.666 ° (longitude) horizontal resolution, is used for the CO₂
 495 simulation with boundary conditions provided by the global model at 2 ° (latitude) x 2.5 ° (longitude) resolution. We made a
 496 restart file with 386.4 ppm for both the global simulation and the nested simulation on 1 January 2009 based on NOAA
 497 ESRL data. Both the global model and the nested-grid model were run twice, driven by the same CO₂ fluxes from January
 498 2009 to February 2013 except that the ODIAC was chosen for the first run and CHRED for the second as the input
 499 fossil-fuel fluxes over the Chinese mainland. Model CO₂ profiles (averages for local hours between 12:00 pm and 13:30 pm)
 500 were presented from January 2010 to February 2013, allowing sufficient time for the high-resolution model to adjust to
 501 transients introduced by the initialization of the model on 1 January 2009. The pressure-weighting function described in
 502 Connor (2008) was applied to convert level-based modeling CO₂ to XCO₂.

503 Fig.3 presents the spatial difference of emissions over the Chinese mainland between CHRED and ODIAC at a
504 horizontal resolution of $1^\circ \times 1^\circ$. The values of emissions from CHRED are mostly larger than those from ODIAC, as shown in
505 Fig. 7, and this difference tends to be large in the eastern part of our study area. In addition, the difference in their total
506 emissions, 10.38 Pg CO_2 for CHRED versus 9.64 Pg CO_2 for ODIAC, is not small. ODIAC is also found to exhibit an
507 overestimation of emissions in large cities compared to CHRED.



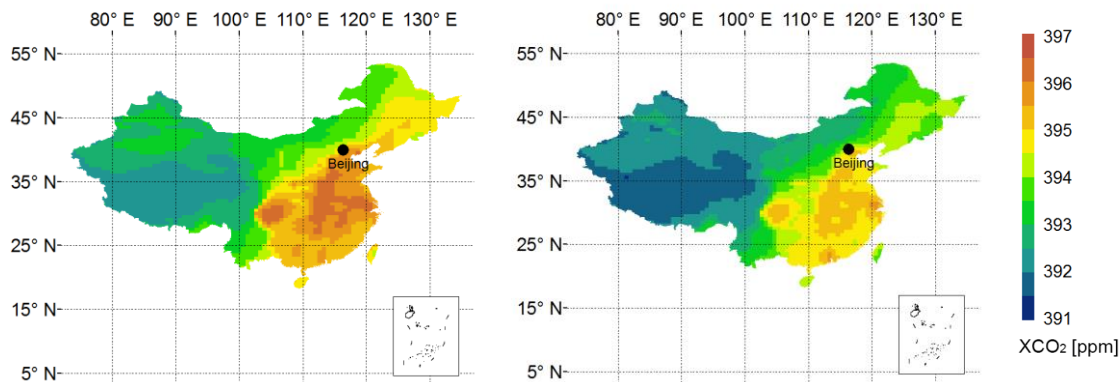
508

509 **Fig. 7. Difference of annual total anthropogenic CO₂ emissions between CHRED and ODIAC in 2012 in China, where the black**
510 **dot represents Beijing, the capital of China.**

511 For each $1^\circ \times 1^\circ$ grid, the corresponding annual CO₂ emissions in the years from 2009 to 2012 were allocated by the ratio
512 of emissions in CHRED to that in ODIAC in 2012. We acquired the new input inventory of CO₂ emissions, CHRED, by
513 scaling the obtained yearly emissions with the ratio of monthly emissions to the yearly ones in ODIAC. In this way, we
514 altered the spatial and temporal distribution, but not at temporal scales finer than monthly. This is expected to be an
515 improvement upon the current ODIAC emission values.

516 The annually averaged XCO₂ simulations, driven separately by CHRED and ODIAC respectively, are calculated and
517 shown in Fig. 8. The impact of emission deviations of CHRED from ODIAC is significant, with XCO₂ from CHRED larger
518 by 0.7 ppm on average over China. There are also obvious differences in spatial patterns, especially in Northwest China,
519 Northeast China, North China and South China. XCO₂ simulations from CHRED are larger by more than 0.7 ppm in most
520 parts east of 100° E with a maximum of 1.4 ppm compared to those from ODIAC. The increase in the annual mean, which
521 should not be ignored, is approximately 1.0 ppm for east of 110° E in the study latitude band. The CO₂ profile dataset from
522 CHRED are used to compare with satellite-retrieved XCO₂ in our following experiments.

523



524

525 **Fig. 8. Annual mean of XCO₂ simulations driven by CHRED (left) and ODIAC (right) in 2012 in China, where the black dot**
 526 **represents Beijing, the capital of China.**

527 We compared GEOS-Chem CO₂ simulations from the global model driven by CHRED with daily mean TCCON data
 528 from 14 TCCON sites (version GGG2014 data version) (Blumenstock et al., 2014; Deutscher et al., 2014; Griffith et al.,
 529 2014a, 2014b; Hase et al., 2014; Kawakami et al., 2014; Kivi et al., 2014; Morino et al., 2014; Sherlock et al., 2014;
 530 Sussmann et al., 2014; Warneke et al., 2014; Wennberg et al., 2014a, 2014b, 2014c). All TCCON measurements between 12
 531 pm and 13:30 pm are used in the comparisons, where GEOS-Chem CO₂ profiles are taken according to the location of
 532 TCCON stations (latitude and longitude) as well as the observing date and transformed to XCO₂ by convolved with the
 533 individual averaging kernel in each station as Wunch (2010) suggested. The statistics results are shown in Table 5.

534 **Table 5. Statistics of comparison between GEOS-Chem CO₂ simulations driven by CHRED and TCCON data from January 2010**
 535 **to February 2013, which includes biases (Δ), the standard deviations (δ), the correlation coefficients (r) and valid days (days) when**
 536 **TCCON data are available. Δ , δ and r are calculated using coincident daily mean data averaged between 12:00 pm and 13:30 pm.**

<u>ID</u>	<u>Station name</u>	<u>Latitude</u>	<u>Longitude</u>	<u>Δ[ppm]</u>	<u>δ[ppm]</u>	<u>r</u>	<u>days</u>
<u>1</u>	<u>Sodankyla</u>	<u>67.37</u>	<u>26.63</u>	<u>2.03</u>	<u>2.00</u>	<u>0.83</u>	<u>269</u>
<u>2</u>	<u>Bialystok</u>	<u>53.23</u>	<u>23.02</u>	<u>0.49</u>	<u>1.84</u>	<u>0.87</u>	<u>196</u>
<u>3</u>	<u>Karlsruhe</u>	<u>49.1</u>	<u>8.44</u>	<u>0.84</u>	<u>1.69</u>	<u>0.84</u>	<u>152</u>
<u>4</u>	<u>Orleans</u>	<u>47.97</u>	<u>2.11</u>	<u>0.44</u>	<u>1.70</u>	<u>0.85</u>	<u>223</u>
<u>5</u>	<u>Garmisch</u>	<u>47.48</u>	<u>11.06</u>	<u>0.65</u>	<u>1.64</u>	<u>0.83</u>	<u>293</u>
<u>6</u>	<u>Park Falls</u>	<u>45.94</u>	<u>-90.27</u>	<u>1.17</u>	<u>2.14</u>	<u>0.75</u>	<u>494</u>
<u>7</u>	<u>Lamont</u>	<u>36.6</u>	<u>-97.49</u>	<u>-0.04</u>	<u>1.22</u>	<u>0.90</u>	<u>642</u>
<u>8</u>	<u>Tsukuba</u>	<u>36.05</u>	<u>140.12</u>	<u>1.43</u>	<u>1.66</u>	<u>0.75</u>	<u>217</u>
<u>9</u>	<u>JPL</u>	<u>34.2</u>	<u>-118.18</u>	<u>-1.30</u>	<u>1.15</u>	<u>0.90</u>	<u>289</u>
<u>10</u>	<u>Saga</u>	<u>33.24</u>	<u>130.29</u>	<u>-0.39</u>	<u>1.65</u>	<u>0.86</u>	<u>159</u>
<u>11</u>	<u>Izana</u>	<u>28.3</u>	<u>-16.48</u>	<u>0.85</u>	<u>1.04</u>	<u>0.90</u>	<u>114</u>
<u>12</u>	<u>Darwin</u>	<u>-12.43</u>	<u>130.89</u>	<u>0.65</u>	<u>0.90</u>	<u>0.88</u>	<u>447</u>
<u>13</u>	<u>Wollongong</u>	<u>-34.41</u>	<u>150.88</u>	<u>0.53</u>	<u>0.83</u>	<u>0.94</u>	<u>347</u>
<u>14</u>	<u>Lauder</u>	<u>-45.04</u>	<u>169.68</u>	<u>0.92</u>	<u>0.42</u>	<u>0.97</u>	<u>370</u>
	<u>Mean</u>			<u>0.59 ± 0.80</u>	<u>1.42 ± 0.50</u>		

537 The results of Table 5 show that the bias ranges from -1.30 to 2.03 ppm for all TCCON sites with standard deviations of
538 the difference varying from 0.42 to 2.14 ppm. The mean standard deviation at the TCCON sites, a measure of the achieved
539 overall precision, from using GEOS-Chem simulations driven by CHRED is 1.42 ± 0.50 ppm which is slightly different
540 from using GEOS-Chem simulations driven by ODIAC (1.41 ± 0.49 ppm). Those validated results with TCCON comparing
541 GEOS-Chem CO₂ simulations driven by CHRED to that by ODIAC indicate that the GEOS-Chem CO₂ simulations driven
542 by CHRED is more likely not to change the global magnitude of CO₂ concentration but rather to depict fine spatial
543 distribution of CO₂ concentration in China.
544

545 **2.4 Aerosol optical depth and surface albedo data**

546 The monthly mean aerosol optical depth (AOD) data were collected from the NASA Earth Observing System's Multi-angle
547 Imaging Spectro-radiometer (MISR) Level 3 Component Global Aerosol Product, downloaded from the website
548 <https://eosweb.larc.nasa.gov/project/misr>. The released GLASS (Glass Land Surface Satellites) albedo product
549 GLASS02B06 (<http://glcf.umd.edu/data/abd/>) is used, which is a gapless, long-term continuous and self-consistent data-set
550 with accuracy similar to that of the Moderate Resolution Imaging Spectrometer (MODIS) MCD43 product (Liu et al., 2013).
551 GLASS02B06 is a daily land-surface shortwave (300-3000nm) broadband albedo product in temporal resolution of eight
552 days.

553 **3 Quantification of agreement of XCO₂ retrievals from four algorithms in the footprints**

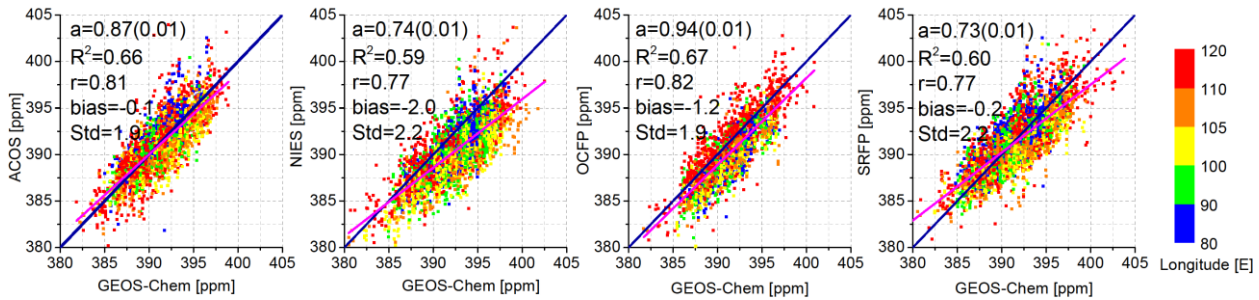
554 We focus on the difference of each footprint XCO₂ retrieval in this section. Comparison of XCO₂ from four algorithms with
555 GEOS-Chem CO₂ simulations driven by CHRED, and pairwise comparisons of XCO₂ between algorithms were calculated
556 as a quantified indicator of their differences.

557 **3.1 Comparisons with GEOS-Chem CO₂ simulations**

558 We used the nested GEOS-Chem CO₂ simulations driven by CHRED as a baseline to quantify the regional consistency of
559 the four algorithms. The collocated model CO₂ profile is averaged over the local hours of 12:00-13:30 pm corresponding to
560 the local time of overpass and locations (latitude and longitude) of GOSAT. To compare XCO₂ retrievals from ACOS, NIES,
561 OCFP and SRFP, corresponding GEOS-XCO₂ data were created by applying averaging kernels from each algorithm to
562 model CO₂ profiles as suggested by Rodgers (2003). Correlation diagrams of XCO₂ between GEOS-Chem (X) and GOSAT
563 (Y) for the four algorithms are shown in Fig. 9. The regression slope (a), the coefficient of determination (R²), the correlation
564 coefficient (r), and biases of GOSAT (Y) from GEOS-Chem(X) are also shown in the inset of each panel.

565 It can be seen from Fig. 9 that the linear fits and the correlations with GEOS-Chem are better for ACOS and OCFP (R²
566 approximately 0.66) than for either NIES or SRFP (R² approximately 0.59). The regression slope is the closest to unity in the

567 OCFP panel (0.94) and is lightly less than OCFP in the ACOS panel (0.87), which means the best similarity in variation. The
 568 slope is less than 0.8 in the NIES and SRFP panels. The bias of GEOS-Chem vs ACOS and SRFP is less than 0.5 ppm while
 569 it is 2 ppm and 1.2 ppm vs NIES and OCFP, respectively.



570

571 **Fig. 9: Correlation diagrams of GOSAT XCO₂ (Y) for the four algorithms vs GEOS-XCO₂ (X). Statistics from linear regression fit**
 572 **are also shown. GEOS-Chem data are selected according to the locations and time of XCO₂ retrievals from the four algorithms in**
 573 **cells. Deep blue solid lines represent 1:1 lines, and the magenta lines demonstrate the best linear regression fit for all samples.**
 574 **Colored points represent XCO₂ for different longitude cells in the study latitude band [37°N, 42°N] shown in Fig.1, where colors**
 575 **for each cell are indicated in the right legend.**

576 Table 6 shows the biases and number of samples used between each algorithm and GEOS-Chem in each cell. It can be
 577 seen that the biases of ACOS and SRFP vs GEOS-Chem in all cells are below 1 ppm, which implies better consistency with
 578 GEOS-Chem regionally than NIES and OCFP. NIES presents 1.2-3.1 ppm lower than GEOS-Chem in all cells excluding
 579 the cell of 115°E, which is likely due to no corrections of the existing systematic biases in the NIES data set (Yoshida et al.,
 580 2013). The bias of OCFP vs GEOS-Chem is larger than 1.2 ppm toward the west of 110°E, while it is 0.1 ppm toward the
 581 east of 110°E. The standard deviations of all the four algorithms with GEOS-Chem range from 1.4 ppm to 2.5 ppm in all
 582 cells.

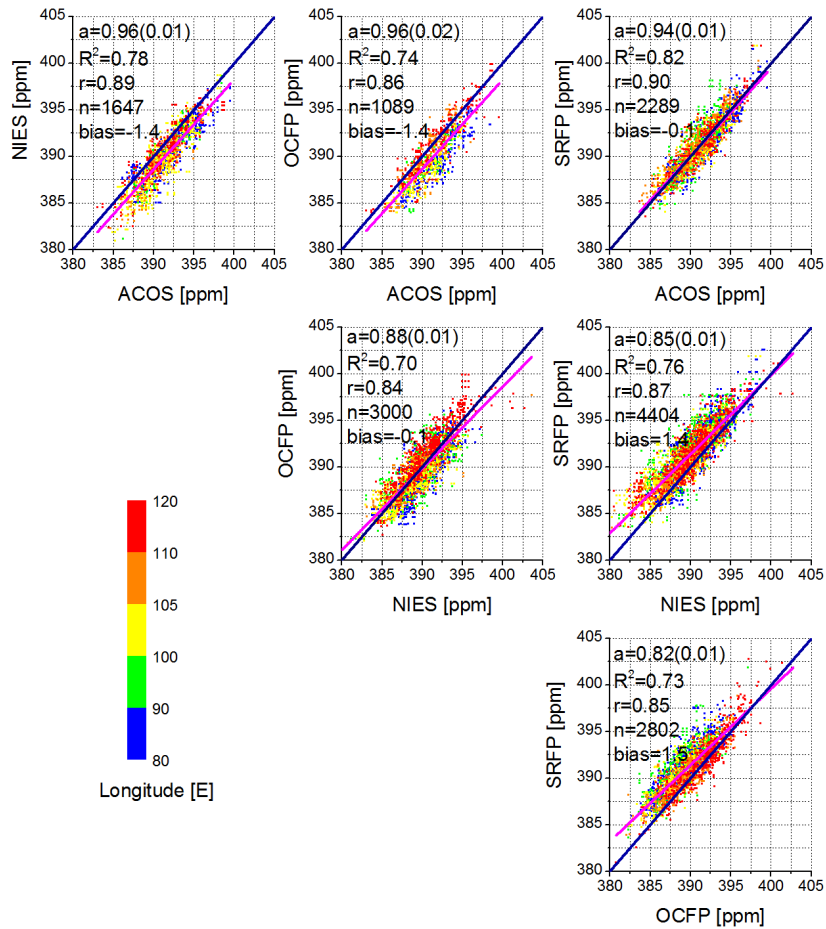
583 **Table 6. The biases (ppm) and their standard deviations (ppm) of the four algorithms vs GEOS-Chem in each cell, where the**
 584 **upper line indicates bias (the corresponding standard deviations in parenthesis) for each algorithm vs GEOS-Chem and the lower**
 585 **line is the available number of used samples. The biases, larger than 1 ppm, are highlighted in bold and underlined.**

Left longitude of cells(°E)	80	85	90	95	100	105	110	115
ACOS	0.7(1.6) 478	0.5(1.6) 179	-0.4(1.4) 316	-0.3(1.5) 303	-0.7(1.7) 629	-0.7(1.7) 599	0.0(2.2) 515	0.5(2.1) 326
NIES	<u>-1.4</u> (1.7) 487	<u>-1.6</u> (1.8) 383	<u>-1.6</u> (1.8) 470	<u>-2.3</u> (2.5) 281	<u>-3.0</u> (1.9) 700	<u>-3.1</u> (2.2) 506	<u>-1.6</u> (2.5) 428	-0.7(2.4) 301
OCFP	<u>-1.8</u> (1.4) 277	<u>-1.8</u> (1.5) 172	<u>-2.2</u> (1.4) 149	<u>-1.2</u> (2.0) 175	<u>-2.3</u> (1.6) 339	<u>-1.5</u> (1.6) 390	-0.1(1.9) 466	-0.1(2.1) 314
SRFP	0.1(1.9) 602	0.0(1.8) 387	0.2(1.7) 388	-0.2(2.0) 271	<u>-1.2</u> (1.9) 571	-0.6(2.7) 659	0.2(2.4) 467	0.0(2.4) 340
EMMA	<u>0.6</u> (1.8) 400	<u>0.2</u> (2.0) 229	<u>-0.4</u> (1.4) 211	<u>-0.2</u> (1.7) 222	<u>-0.8</u> (1.8) 484	<u>-1.0</u> (2.0) 460	<u>-0.1</u> (2.1) 453	<u>-0.1</u> (2.1) 337

586

587 **3.2 Pairwise comparisons of XCO₂ between algorithms**

588 We made comparisons of geometrically and timely matching pairs XCO₂ between algorithms in each cell. The pairs of
 589 XCO₂ retrievals were matched between two algorithms timely in the same day and geometrically located within $\pm 0.01^\circ$ in
 590 latitude and longitude. Figure 6 shows pairwise comparisons of XCO₂ retrievals between two algorithms that demonstrate
 591 the regression slope (a), the coefficient of determination (R^2), the correlation coefficient (r), the number of matching pairs (n)
 592 and the biases between every pair of algorithms.
 593



594
 595 **Fig. 10: Algorithm correlation diagrams and statistical characteristics (insets of panels). GOSAT-Y observations were selected**
 596 **over land within $\pm 0.01^\circ$ latitude/longitude of each GOSAT-X observation and in the same day. Deep blue solid lines represent 1:1**
 597 **lines, and the magenta ones display the best linear regression fit for all observations. Colored points represent XCO₂ for different**
 598 **cells: blue-[80 E, 90 E], green-[90 E, 100 E], yellow-[100 E, 105 E], orange-[105 E, 110 E], and red-[110 E, 120 E] in the study**
 599 **latitude zone [37 N, 42 N].**

600 It can be seen from Fig. 10 that ACOS generally demonstrates the best agreement with other algorithms (top panel).
 601 OCFP generally presents biases larger than 1.4 ppm with other algorithms except for 0.1 ppm compared to NIES. It can also

602 be seen from the colored points in Fig. 10 that matching pairs of XCO₂ for OCFP vs ACOS and SRFP mostly concentrated
 603 along the 1:1 line in the eastern cells of 105-120 °E (orange and red points) but drifted from the 1:1 line in the western cells
 604 of 80-100 °E (blue and green points).

605 The differences (biases) of matching pairs (the number ranging from 11 to 945) of XCO₂ between two algorithms,
 606 moreover, were calculated for each cell as shown in Table 7, and the totally averaged absolute differences of matching pairs
 607 of XCO₂ for an algorithm with the other algorithms were also calculated in each cell as shown in Table 8.

608 It can be found from Table 7 that the difference is mostly less than 1 ppm in those eastern cells with a longitude greater
 609 than 105 °E, and their consistency can be seen in Fig. 10 (red points between 110-120 °E) as well. The differences that are
 610 larger than 2 ppm are located in western cells with longitudes less than 105 °E, and these differences are mostly shown in
 611 OCFP vs other algorithms. The total differences shown in Table 8, moreover, indicate that the differences of the four
 612 algorithms tend to be similar to the results of matching pairs of XCO₂ (Table 7), and NIES presents the largest difference up
 613 to 1.6 ppm in the western cells of 95 °E.

614 **Table 7. Differences (ppm) between two algorithms (column algorithm minus row algorithm) and the corresponding standard**
 615 **deviation (ppm) for each cell, where values in parentheses are the corresponding standard deviations. The differences, larger than**
 616 **1.5 ppm, are highlighted in bold and underlined.**

	*	NIES	OCFP	SRFP	EMMA	*	NIES	OCFP	SRFP	EMMA
ACOS		-1.4(1.2)	<u>-2.6</u> (1.2)	-0.5(1.2)	0.2 (1.0)		<u>-1.6</u> (1.6)	<u>-2.0</u> (1.1)	-0.2(1.2)	0.2 (1.1)
NIES	80		-0.9(1.4)	1.1(1.4)	<u>1.7</u> (1.5)	100		-0.4(1.4)	1.4(1.5)	<u>1.6</u> (1.4)
OCFP	°E			<u>2.0</u> (1.2)	<u>2.6</u> (1.5)	°E			<u>1.7</u> (1.3)	<u>1.9</u> (1.4)
SRFP					0.4 (1.1)					0.3 (1.1)
ACOS		<u>-2.0</u> (1.3)	<u>-1.9</u> (1.2)	-0.1(1.2)	0.5 (0.9)		<u>-1.6</u> (1.3)	-0.6(1.4)	0.2(1.2)	0.2 (0.9)
NIES	85		-0.4(1.6)	1.5(1.3)	<u>2.0</u> (1.5)	105		0.2(1.5)	1.2(1.3)	<u>1.5</u> (1.3)
OCFP	°E			<u>2.3</u> (1.4)	<u>2.7</u> (1.5)	°E			1.0(1.3)	1.0 (1.0)
SRFP					0.2 (1.2)					0.2 (0.9)
ACOS		-1.2(1.1)	<u>-1.7</u> (1.1)	0.8(1.4)	0.5 (0.8)		-1.2(1.3)	-0.9(1.4)	0.0(1.4)	0.4 (1.1)
NIES	90		-0.8(1.4)	<u>2.0</u> (1.4)	1.5 (1.2)	110		0.7(1.3)	1.5(1.6)	1.5 (1.3)
OCFP	°E			<u>2.4</u> (1.5)	<u>2.0</u> (1.3)	°E			0.5(1.2)	0.7 (1.0)
SRFP					-0.1 (1.1)					0.0 (1.3)
ACOS		<u>-3.0</u> (1.1)	-0.9(1.7)	-0.3(1.2)	0.0 (1.1)		-0.6(1.3)	0.1(1.0)	-0.1(1.0)	0.5 (1.0)
NIES	95		0.5(2.1)	1.3(2.0)	<u>1.7</u> (1.9)	115		0.8(1.5)	0.9(1.3)	1.3 (1.5)
OCFP	°E			<u>1.8</u> (1.6)	1.4 (1.1)	°E			0.2(1.3)	0.5 (1.0)
SRFP					0.2 (1.3)					0.6 (0.9)

617 The columns labeled with * represent the left longitude of cells (°E).

618 **Table 8. The average of the absolute differences (ppm) and standard deviation (ppm) of the target algorithm (in column) matching**
 619 **all other algorithms for each cell. Values in parentheses are the corresponding standard deviations. The differences, which are**
 620 **larger than 1.5 ppm, are highlighted in bold and underlined.**

Left longitude of cells(°E)	80	85	90	95	100	105	110	115
ACOS	1.5 (0.8)	1.4 (0.7)	1.2 (0.4)	1.6 (1.0)	1.4 (0.6)	1.1 (0.4)	1.1 (0.2)	0.9 (0.2)

NIES	1.6(0.2)	1.8(0.4)	1.6(0.4)	2.2(0.6)	1.6(0.3)	1.5(0.3)	1.5(0.3)	1.3(0.2)
OCFP	2.2(0.6)	2.1(0.6)	1.9(0.5)	1.7(0.2)	1.7(0.4)	1.2(0.1)	1.1(0.1)	1.0(0.2)
SRFP	1.3(0.5)	1.4(0.7)	1.6(0.8)	1.4(0.6)	1.3(0.5)	1.1(0.3)	1.2(0.4)	1.0(0.2)
EMMA	1.6(0.9)	1.6(1.0)	1.3(0.6)	1.3(0.6)	1.3(0.6)	1.1(0.5)	1.1(0.4)	1.0(0.4)

621

Left longitude of cells(°E)	80	85	90	95	100	105	110	115
ACOS	1.3(1.1)	1.2(1.0)	1.0(0.7)	1.4(1.2)	1.2(0.9)	1.0(0.7)	0.9(0.6)	0.7(0.5)
NIES	1.1(0.7)	1.3(0.9)	1.2(0.9)	1.6(1.2)	1.1(0.8)	1.1(0.8)	1.1(0.8)	0.9(0.6)
OCFP	1.5(1.1)	1.4(1.0)	1.4(1.0)	1.3(0.9)	1.2(0.9)	0.9(0.6)	0.8(0.6)	0.8(0.6)
SRFP	1.1(0.9)	1.2(1.0)	1.4(1.1)	1.2(0.9)	1.1(0.8)	0.9(0.6)	1.0(0.7)	0.8(0.5)

622

623 To summarize the quantification and analysis in this section, XCO₂ retrievals from two algorithms, ACOS and SRFP
624 are mostly consistent, and the bias of ACOS from GEOS-Chem is the least among the four algorithms. The difference of
625 XCO₂ from cross-comparing four algorithms tends to be less in cells east of 100°E than that in the cells west of 100°E.

626 4 Comparison of the spatio-temporal pattern revealed by XCO₂ from the four algorithms and simulation

627 We used a combination of sine and cosine trigonometric functions to statistically fit the seasonal variation of XCO₂, which
628 was originally proposed by Keeling et al. (1976) and has been applied extensively in many studies (Thoning et al. 1989;
629 Kulawik et al., 2016; Lindqvist et al., 2015; Zeng et al., 2016; He et al., 2017). Better attributions are thus obtained for XCO₂
630 variation in the seasonal cycle and in spatial background patterns by filtering the noise and filling gaps in the original XCO₂
631 data.

632 Firstly, the monthly averaged XCO₂ was calculated in each cell using XCO₂ retrievals; then the fit function (Keeling,
633 1976), expressed as the following equation [1], was applied to the monthly averaged XCO₂ from March, 2010 to February,
634 2013 for the four algorithms and GEOS-Chem.

$$635 \quad X(t) = A_1 \sin 2\pi t + A_2 \cos 2\pi t + A_3 \sin 4\pi t + A_4 \cos 4\pi t + A_5 + A_6 t \quad [1]$$

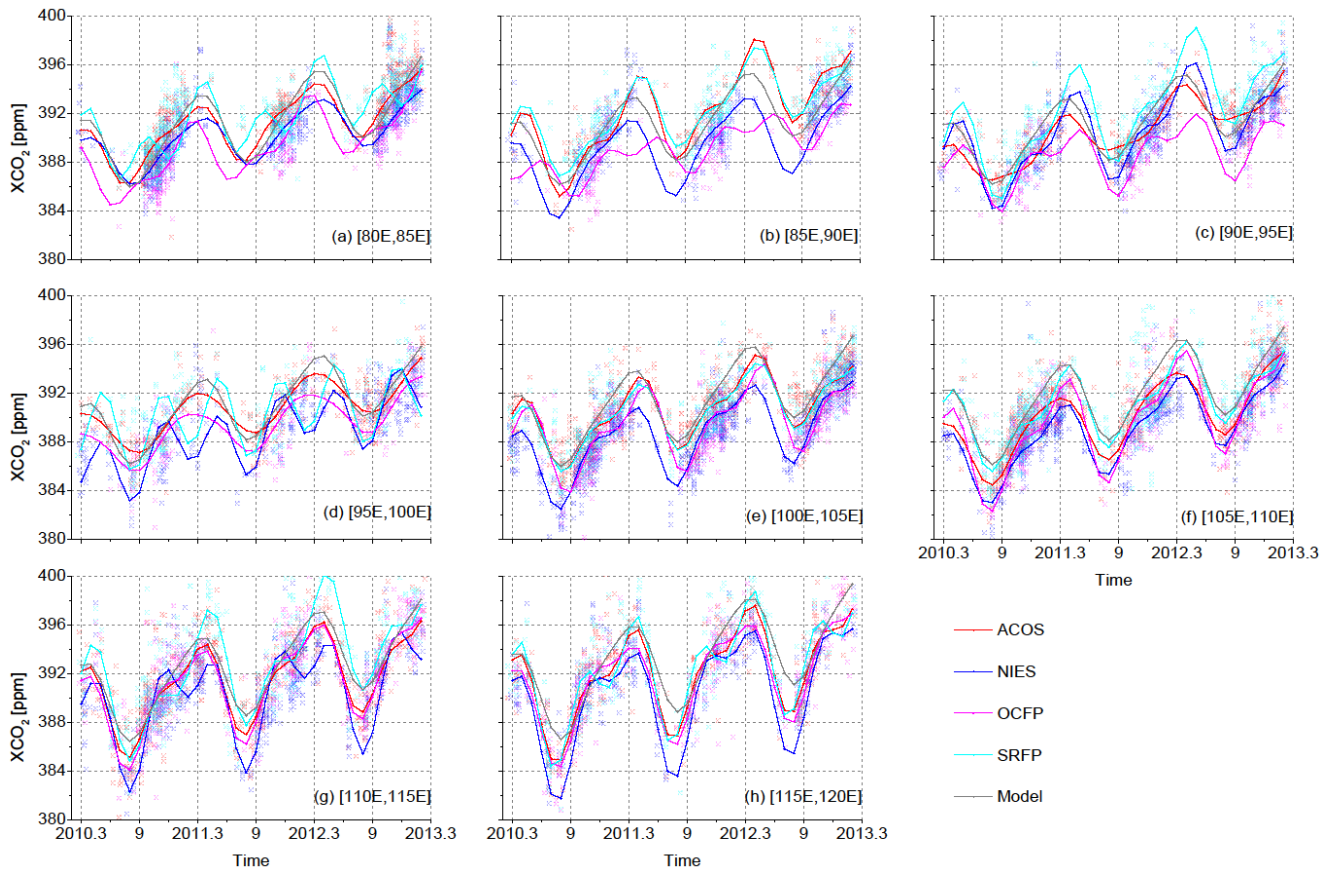
636 where t represents elapsed time in years, A₁-A₄ are the coefficients determining the seasonal cycle, A₅ represents the initial
637 state of XCO₂ with seasonal variation removed, which can be regarded as the corresponding background concentration, and
638 A₆ is the slope of the linear part in the yearly increase ignoring the minor non-linear part. To derive A₁-A₆ with the above
639 formula, least squares were applied to fit the input monthly weighted means with the corresponding standard deviations as
640 measures of errors. The monthly weighted means (e.g., X(t)) and the corresponding standard deviations in each cell were
641 calculated with the weights inversely proportional to the square of retrieval uncertainty in each observation point.

642 The accuracy of fitting X(t) depends on the number of gaps in the available XCO₂ retrievals in time and in space
643 resulting from the filtering mechanism for quality controlling. We introduce the Pearson's correlation, hereafter referred to
644 as R, between the input and the predicted results from equation [1] and the unit weighted mean square error, hereafter

645 referred to as σ , in fitting as an uncertainty to judge whether the fitting results are reasonable or not. In addition, we applied
 646 equation [1] to the GEOS-Chem dataset, which has been converted to XCO_2 as Connor (2008) suggested. Since atmospheric
 647 transport models do not share the same error sources with satellite retrieval algorithms and produces continuous simulations
 648 without data gaps, GEOS-Chem provides helpful a priori information for reference.

649 4.1 Seasonal variation of XCO_2 retrievals

650 The time series in each cell are acquired for each algorithm using the above formula [1]. The monthly fitted XCO_2 from
 651 March 2010 to February 2013 in each cell for the four algorithms as well as GEOS-Chem is shown in Fig. 11. The seasonal
 652 amplitudes (the difference between seasonal cycle maximums and minimums) and uncertainty of the fitting function as
 653 described by R and σ above are demonstrated in Table 9.



654

655 **Fig. 11: The time series from March 2010 to February 2013 in eight cells from the western cell of (a) to the eastern end cell of (h),**
 656 **where colored lines represent the fitting seasonal change trend of the four XCO_2 datasets from the four algorithms, and the**
 657 **colored points represent single XCO_2 retrievals corresponding to four algorithms according to line color: red is for ACOS, blue for**
 658 **NIES, magenta for OCFP and cyan for SRFP. The gray line is the fitting seasonal change trend of XCO_2 simulated by GEOS-**
 659 **Chem.**

660 Table 9: Results of fitted seasonal cycle and the corresponding uncertainty of the fitting results for each cell in the study latitude
 661 band for four algorithms and GEOS-Chem, The symbols “-“ means that filtered results are not available due to large uncertainty
 662 judged by R and σ . **R**, the correlation coefficient between fitted XCO₂ and monthly averaged original XCO₂ in each cell, less than
 663 **0.80**, and **σ** , the unit weighted mean square error in fitting, not less than 3.0, are highlighted in bold and underlined.

Left longitude of cells (°E)	80	85	90	95	100	105	110	115
Seasonal cycle amplitude (ppm)								
ACOS	5.1	7.8	3.7	4.0	6.6	5.9	8.0	9.3
NIES	4.3	6.9	7.8	-	7.1	6.4	9.5	10.7
OCFP	5.3	3.5	-	3.9	7.7	9.2	8.4	8.6
SRFP	6.3	6.5	8.9	-	5.9	7.4	10.4	10.7
GEOS-Chem	6.3	5.9	5.7	5.6	6.5	6.9	7.2	7.9
σ (Unit weight mean square error in fitting)(ppm)								
ACOS	1.2	1.6	1.6	0.6	1.1	1.2	0.4	1.0
NIES	0.7	1.1	1.0	<u>3.0</u>	1.1	1.1	1.5	1.3
OCFP	0.7	0.9	1.5	1.4	1.9	1.1	0.8	0.9
SRFP	1.6	0.7	1.3	<u>3.3</u>	0.8	0.8	1.0	1.0
GEOS-Chem	0.1	0.1	0.1	0.1	0.1	0.1	0.1	0.1
R (Correlations between fitted XCO ₂ and monthly averaged original XCO ₂ in each cell)								
ACOS	0.92	0.92	0.91	0.95	0.91	0.91	0.98	0.94
NIES	0.89	0.91	0.94	<u>0.68</u>	0.96	0.95	0.89	0.92
OCFP	0.90	0.84	<u>0.79</u>	0.84	0.93	0.93	0.93	0.96
SRFP	0.83	0.94	0.92	<u>0.40</u>	0.95	0.94	0.93	0.90
GEOS-Chem	1.00	1.00	0.99	0.99	0.99	0.99	0.99	0.99

664

665 Viewing the attribution of XCO₂ in each cell from Fig. 11 and Table 9, we can find that the seasonal variations from all
 666 XCO₂ retrievals generally show similar changing trends, except for one extra seasonal cycle maximum being misidentified in
 667 some cases mainly due to weaker data constraints for fitting. The timely changing patterns (indicated by seasonal cycle
 668 phases) of all algorithms demonstrate better agreement in the eastern four cells from 100°E to 115°E than those in the
 669 western four cells from 80°E to 95°E. The correlation coefficients of fitting XCO₂ in Table 9 are also significantly greater in
 670 the eastern four cells than those in the western four cells. As a result, the longitude 100°E tends to be a regional border
 671 presenting better consistency of XCO₂ among the four algorithms in its eastern cells than those in its western cells.

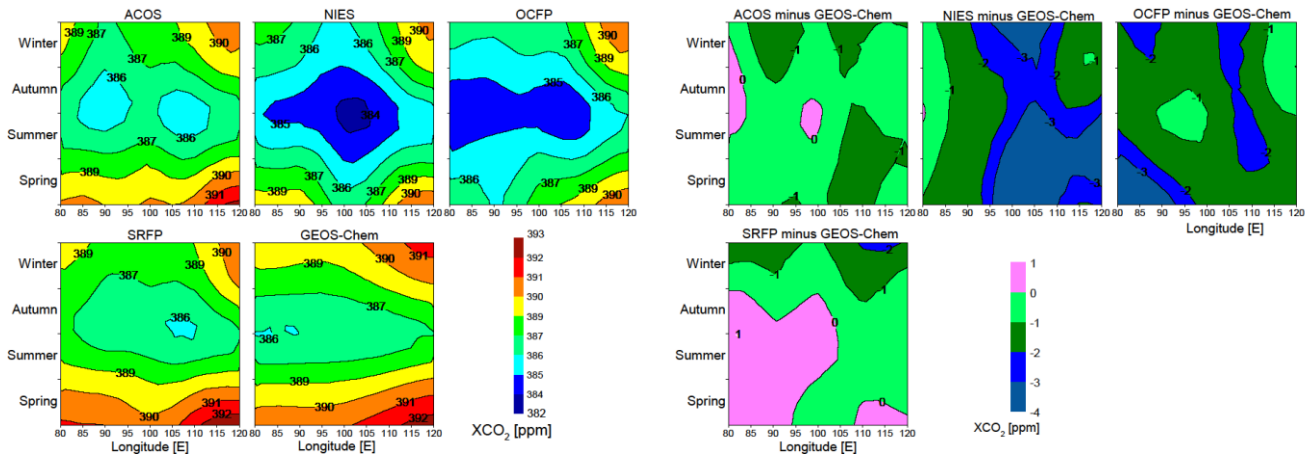
672 Comparing XCO₂ from the four algorithms with GEOS-Chem, one specific result is presented in the eastern-most two
 673 cells from 110°E to 120°E, in which the seasonal amplitudes of XCO₂ are significantly higher from the four algorithms while
 674 the magnitudes of XCO₂ in summer are lower than those from GEOS-Chem as shown in Table 9 and Fig. 11. There is strong

675 CO₂ absorption from farming activities of wheat and corn in the summer (Lei et al., 2010) and anthropogenic CO₂ emission
676 from extra winter heating in these eastern cells. This result is in agreement with an investigation of results over the whole
677 Chinese mainland (Lei et al., 2014) and at 120-180°E over the globe (Lindqvist et al., 2015), which is likely due to the
678 underestimated widespread bio-ecological CO₂ uptake changes that occurred over the past 50 years in atmospheric transport
679 models (Graven et al., 2013).

680 The XCO₂ values from NIES (blue in Fig. 11) are overall lower than those from the other algorithms, which is due to
681 the uncorrected systematic errors -1.2 ppm (refer to Table 4). The seasonal variations from OCFP (magenta in Fig. 11) are
682 abnormal compared to the overall seasonal changing trend of XCO₂ in cells west of 100°E presented for the other three
683 algorithms. The seasonal amplitudes of OCFP presented in Table 9, moreover, are abnormally the lowest in a cell (85-90°E)
684 and the highest in a cell (105-110°E). SRFP and NIES show two abnormal peaks in a cycle of a year in the cell of 95°E,
685 while some large values of σ and small values of R, shown in bold in Table 9, indicate poor fitting mostly in the same cell
686 (95-100°E). These results are likely induced by large gaps in the available XCO₂ data in time series, which leads to a poor
687 fitting constraint.

688 **4.2 Spatio-temporal pattern of detrended XCO₂**

689 We calculated the seasonal averages of the XCO₂ background concentration in each cell after removing the linear yearly
690 increase using the fitting time series of XCO₂ for the four algorithms and GEOS-Chem. The spatio-temporal continuous
691 pattern of background XCO₂ was mapped by Linearly Interpolate Triangulation (Watson et al., 1984) using the seasonal
692 averages of XCO₂ background concentration in each cell for four algorithms and GEOS-Chem, as shown in Fig. 12 (on the
693 left). The spatio-temporal patterns of the differences of detrended XCO₂ to GEOS-Chem simulations for the four algorithms
694 are mapped respectively and are shown in Fig. 12 (on the right).



696

697 **Fig. 12: The spatial (in the study latitude band) and temporal (in seasons) changing patterns of detrended XCO₂ from ACOS,**
 698 **NIES, OCFP, SRFP retrievals and GEOS-Chem simulations (left) and the differences of detrended XCO₂ to GEOS-Chem for**
 699 **between-ACOS, EMMA, NIES, OCFP and SRFP and GEOS-Chem.**

700 It can be seen from Fig. 12 (on the left) that the spatio-temporal patterns from the three algorithms of ACOS, NIES and
 701 SRFP are generally similar, with an increase spreading outward from the center of each diagram and with the lowest XCO₂
 702 located approximately at 95 °E-105 °E and during the period of summer-autumn; meanwhile, OCFP and GEOS-Chem show a
 703 similar spatio-temporal pattern where the lowest value is not the center. Two common characteristics of XCO₂ spatio-
 704 temporal changes from the four algorithms and GEOS-Chem can also be found: (1) the seasonal changes of XCO₂ are the
 705 same in any of the cells, with lower XCO₂ in summer and autumn than that in spring and winter; and (2) spatial changes of
 706 XCO₂ generally demonstrate larger XCO₂ in the eastern cells than those in the western cells in all seasons. A similarly high
 707 level is captured by ACOS, NIES and SRFP generally in the western deserts with lower CO₂ emissions compared to the
 708 eastern cells with abundant emissions. This feature is especially distinct from ACOS while OCFP and GEOS-Chem both
 709 show an increasing trend from west to east in any season.

710 Comparing the difference to GEOS-Chem (on the right in Fig. 12), the spatio-temporal pattern of ACOS and SRFP
 711 generally demonstrate the smallest values mostly ranging from -1 ppm to 1 ppm. XCO₂ values from both NIES and OCFP
 712 are smaller than GEOS-Chem in space and time, while the XCO₂ difference is mostly 1-3 ppm for NIES and 2 ppm for
 713 OCFP. Regionally, the differences tend to be larger in the western cells than those in the eastern cells for satellite retrievals,
 714 except for OCFP.

715 ~~To summarize the quantification and analysis in this section, the spatio-temporal pattern of ACOS tends to be~~
 716 ~~inconsistent with SRFP. Figure 8 shows two common characteristics among ACOS, NIES, SRFP and EMMA: (1) XCO₂ is~~
 717 ~~lower in summer and autumn but higher in spring and winter. (2) XCO₂ is higher west of 90 °E and east of 110 °E, while it is~~
 718 ~~lower in cells 90 °E-110 °E. In addition, XCO₂ values from NIES and OCFP are lower than those from other algorithms,~~
 719 ~~especially in summer and autumn. A similarly high level is captured by ACOS, EMMA, NIES and SRFP generally in the~~

720 ~~western deserts with lower CO₂ emissions compared to the east, which has abundant emissions. This is distinct from ACOS~~
721 ~~and EMMA, while OCFP and GEOS-Chem both show an increasing trend from west to east in any season.~~

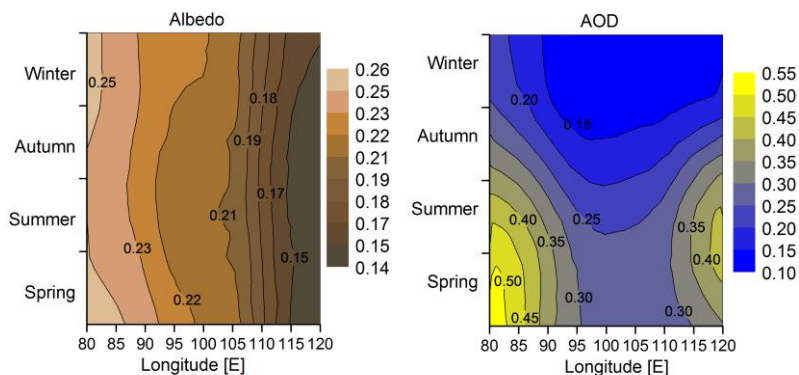
722 **5 Discussion**

723 In this section, an investigation was made into the most likely attribution of regional inconsistency, i.e., aerosols and albedo,
724 and an additional ~~evaluation-comparison~~ was made ~~of-with~~ the latest released ACOS V7.3, the newer version of ACOS data
725 retrieved by the OCO-2 algorithm, using GEOS-Chem simulations and retrievals from other algorithms including ACOS
726 V3.5, NIESV02.21, OCFP V6.0 and SRFP V2.3.7.

727 **5.1 Discussion of albedo and aerosol effects for XCO₂ retrieval**

728 The above quantification and analyses indicate that generally good agreements are achieved among the four data sets in the
729 eastern cells, while three out of four GOSAT-XCO₂ data sets present abnormal high concentrations in the western cells. It
730 has been known that aerosols are the most important factor inducing errors in satellite-retrieved XCO₂ (Guerlet et al., 2013;
731 Oshchepkov et al., 2013; Yoshida et al., 2013; O'Dell et al., 2012), while ~~estimations of Aerosol Optical Depth (AOD)~~AOD
732 in GOSAT full physics CO₂ retrieval algorithms are ~~is~~ greatly affected by high surface albedo because of atmospheric
733 multiple scattering of light and the optical lengthening effect~~the optical lengthening effect~~. For that reason, we investigate
734 the spatial and temporal characteristics of aerosols and albedo in our study latitude band to probe the reason why high
735 inconsistency of XCO₂ retrieval algorithms appears in western cells rather than in eastern cells with intensive human
736 activities.

737 The spatial and temporal characteristics of shortwave broadband (300-3000nm) albedo from GLASS albedo products
738 and AOD at 555 nm from MISR aerosol products with seasons in the study area are revealed as shown in Fig. 13, in which
739 they are mapped by the same method as Fig. 12. The seasonal mean AOD and albedo were calculated in spring (MAM),
740 summer (JJA), autumn (SON), and winter (DJF) using the monthly mean AOD and black sky shortwave albedo from
741 January 2010 to December 2012 for every cell.



742

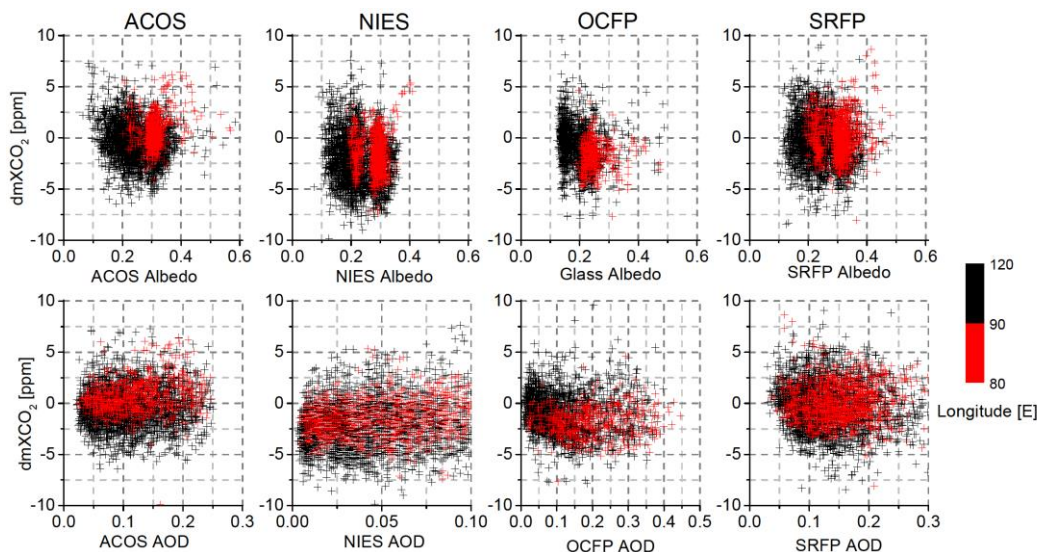
743 | **Fig. 13: The temporal and spatial patterns of black sky shortwave broadband (300-3000nm) albedo (left) and AOD at 555 nm**
 744 | **(right). Colors represent albedo (left) and AOD (right).**

745 As shown in Fig. 13, albedo shows small temporal variation with a decreasing trend from west to east. In contrast with
 746 albedo, AOD follows a clear seasonal pattern with a higher level in spring and summer than in autumn and winter. The uplift
 747 of AOD in spring and summer is due to the higher frequency of Asian sand and dust storms for cells west of 105 °E. The
 748 main contributors to aerosol loading east of 110 °E are emissions from urban fugitive dust/fly ash, dust plumes from deserts
 749 in the western and northern China such as the Taklimakan deserts, industrial activities and residential heating (Zhang et al.,
 750 2012). For this reason the inconsistency of XCO₂ from the four algorithms, which tends to be higher in spring and summer
 751 than in autumn and winter in the Taklimakan Deserts in western cells shown in the results above, is likely induced by the
 752 combined effect of high aerosol and high brightness surface (high surface albedo) on retrieval uncertainty.

753 We discussed the influences of albedo and AOD on XCO₂ retrievals from ACOS, NIES, OCFP and SRFP in further.
 754 Fig. 14 plots the scatters of albedo and AOD with the differences between GEOS-XCO₂ data (created in section 3.1) to
 755 XCO₂ retrievals, hereafter referred to as dmXCO₂, for ACOS, NIES, OCFP and SRFP. The albedo data obtained from
 756 GLASS02B06 is used for OCFP as there are no albedo data available from its released data product.

757 Fig. 14 shows that dmXCO₂ of both ACOS and NIES demonstrate a slightly decreasing trend with albedo whereas
 758 slightly increasing trend with AOD. The dmXCO₂ of ACOS tend to be larger in 80 °E -90 °E of deserts with high albedo than
 759 that in other regions. The dmXCO₂ of OCFP demonstrate a clear decreasing trend with albedo and AOD comparing to the
 760 other algorithms. The dmXCO₂ of SRFP basically does not show a clearly dependence on either albedo or AOD. We further
 761 investigated the standard deviation of dmXCO₂ by a variation of the bin-to-bin dmXCO₂ with albedo and AOD. dmXCO₂ is
 762 averaged by surface albedo within 0.05 albedo bins and AOD within 0.05 AOD bins, respectively. The standard deviation of
 763 the mean dmXCO₂ in each 0.05 albedo (AOD) bins, i.e. a measure of the bin-to-bin dmXCO₂, is calculated. It is found that
 764 the dmXCO₂ for the four algorithms change with both albedo and AOD in bin-to-bin. In the whole study area, the standard
 765 deviation in albedo is the largest for OCFP, up to 0.7 ppm, while that is smaller from ACOS, NIES and SRFP, 0.4 ppm, 0.3
 766 ppm and 0.2 ppm, respectively. The standard deviation of dmXCO₂ in AOD is larger for SRFP (0.5 ppm) than those for

767 ACOS (0.2 ppm), NIES (0.3 ppm) and OCFP (0.4 ppm). Viewing to the deserts (80°E -90°E), the standard deviation in
 768 albedo is the largest from NIES (1.5 ppm), and the smallest from OCFP (0.2 ppm) while they are 1.0 ppm and 0.5 ppm for
 769 ACOS and SRFP, respectively. The standard deviations in AOD, however, are similar (0.2-0.4 ppm) in this area. As a result,
 770 OCFP tend to be more sensitive to albedo and AOD compared to other algorithms. In the deserts, NIES are the most
 771 sensitive XCO₂ retrievals to surface albedo and OCFP the least.



772
 773 Fig. 14: Scatter plots of the differences (dmXCO₂) between GEOS-XCO₂ to ACOS, NIES, OCFP and SRFP respectively, with
 774 respect to albedo (the upper panels) and AOD (the lower panels). Colored points represent the data from different cells: red-[80°E,
 775 105°E], black-[105°E, 120°E] in the study latitude zone [37°N, 42°N]. Colored solid lines display the corresponding linear
 776 regression trend line for the total points. Albedo and AOD are extracted from data products of the retrieval algorithms except
 777 albedo data in OCFP in which GLASS data are used.

778 Fig. 15, moreover, demonstrates the influence of albedo and AOD on the standard deviation (STD) of XCO₂ from four
 779 algorithms at the same footprints (timely in the same day, geometrically located within ±0.01° in space). Averaged albedo
 780 (the left panels) and AOD (the right panels) of the four algorithms are used whereas the averaged albedo is obtained only
 781 using three attached albedo in the algorithms except OCFP.

782 The increasing trends of STD with both albedo and AOD can be seen from Fig. 15. The mean STD is 1.3 ppm in the
 783 western cells (80°E -90°E) where albedo is mostly within 0.25-0.35. This STD is lightly larger than that (1.0ppm) in eastern
 784 cells (90°E-120°E) where albedo is comparatively smaller (mostly within 0.15-0.25). It is found from the statistics presented
 785 in Fig. 15 that the correlation coefficients of STD with albedo and that with AOD is almost the same (both are 0.3) for all the
 786 data. Particular influence from albedo in desert over the western cells can be clearly observed. These results indicate that the
 787 inconsistency of XCO₂ retrievals from four algorithms tend to be increase with the enlargements of albedo and AOD so as to
 788 imply that uncertainty of satellite-retrieved XCO₂ should be mostly alerted with the elevations of albedo and AOD.

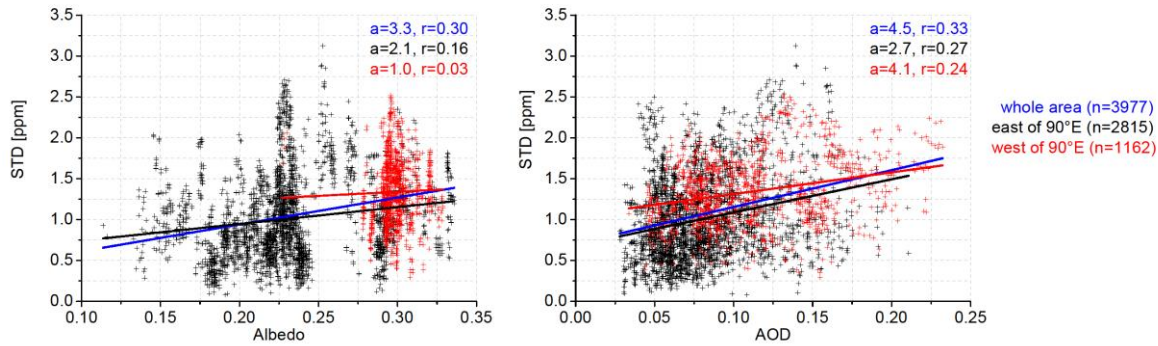


Fig. 15: Scatter plots of the standard deviation (STD) of XCO₂ from the four algorithms to albedo (the left panel) and AOD (the right panel). Colored points represent different cells: red-[80 °E, 105 °E], black-[105 °E, 120 °E] in the latitude zone [37 °N, 42 °N]. Colored solid lines display the corresponding linear regression trend line for the scatter plots with the regression slope (a) and the correlation coefficient (r) also presented. n is the number of samples. Albedo is the mean surface albedo in 0.75-um band from the three algorithms including ACOS, NIES and SRFP. AOD is the mean AOD in 0.75-um band from the four algorithms.

From the above quantification and analysis in previous sections, the pairwise differences between OCFP and other algorithms are 0.5± ppm higher west of 105 °E than east of that, with a difference of 1.2±.6 ppm over the whole study area. The obvious regional characteristic probably relates to the assumption of a uniform cirrus profile based on latitude in the retrieval algorithm (GHG-CCI group at University of Leicester, 2014), which is, however, unlikely to be reasonable in our study area. There exists a large amount of high clouds over the Tibetan Plateau (Chen et al., 2005), which is located south of the study cells of 80 °E to 105 °E. The humidity and atmospheric structure are mainly affected by the Tibetan Plateau, and there is a large difference in the cirrus profile between the western cells and the eastern cells over our study area (Wang et al., 2012), which indicates that a uniform profile by latitude will inevitably introduce errors.

The regional pairwise difference between NIES and other algorithms is 1.6 ppm on average, is up to 1.6 ppm, which is distinctly high among all the algorithms. Considering the complicated geographic environment in the study area, this distinct difference is likely related to the presumptions from NIES algorithm in aerosol profiles and properties adopted from an aerosol transport model (Table 4), in which cirrus clouds are ignored and little information from observations is used in the retrieving process.

With the satellite-observed spectrum used for simultaneously retrieving water and clouds, ACOS sets the initial aerosol types and AOD based on a priori information from aerosol reanalysis data. On the other hand, SRFP handles aerosol based on a comprehensive characterization of aerosol properties, including aerosol number density, size distribution and aerosol height. Both of the above two mechanisms function well since ACOS and SRFP are generally demonstrated to provide relatively better performance.

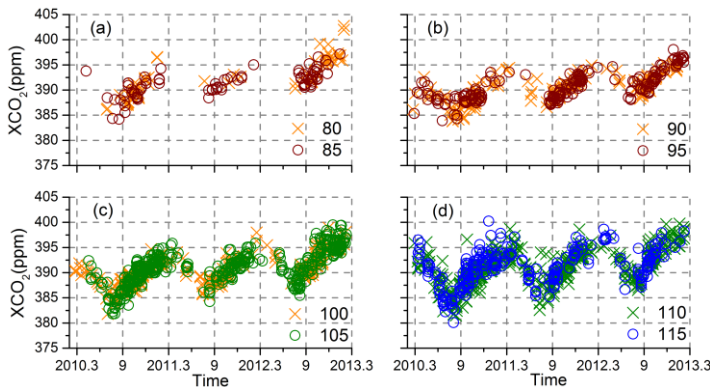
Noticing that all algorithms differ in simulating scattering in the atmosphere, such as in the aerosol models, the influence of scattering on retrieved XCO₂ is too significant to be ignored, as demonstrated from this study. Since satellite products from different retrieval algorithms in general agree with each other, there is no denying that satellite XCO₂

817 retrievals have the potential to provide more accurate XCO₂ data. Optimization in the handling of aerosol scattering will
818 improve the precision and accuracy of satellite XCO₂ retrievals in the future.

819 5.2 Additional comparison with evaluation of the latest released ACOS V7.3

820 We collected ACOS V7.3 (<http://CO2.jpl.nasa.gov>) too, the latest version of the ACOS data (GES DISC, 2017). We add the
821 cross-comparisons of this version of the data set and other data sets including GEOS-Chem, ACOS V3.5, NIES V02.21,
822 OCFP V6.0 and SRFP V2.3.7 in this section. ACOS V7.3 was created by applying the XCO₂ retrieval algorithms of OCO-2
823 to GOSAT. Within the algorithm code of ACOS V3.5, the OCO-2 algorithm generating ACOS V7.3 data makes some
824 changes in parameter settings, such as the surface pressure a priori constraint and cloud ice properties, and it updates the
825 manners of data processing, for example, the bias corrections and filtering mechanism (GES DISC, 2017).

826 ~~The available data points, a total of 1980, were shown from March 2010 to February 2013 in Fig. 10, where different colors~~
827 ~~and symbols in each panel represent the left longitude of cells into which retrievals fall. In cells west of 90 °E, there are a few~~
828 ~~data points showing abnormal concentrations as high as above 400.0 ppm, which is higher than that of data points in the east,~~
829 ~~where there are strong anthropogenic CO₂ emissions.~~



830 **Fig. 10. The time series of data points from ACOS V7.3 during the period from March 2010 to February 2013. Different symbols**
831 **in each panel represent the left longitude of the cell into which a data point falls.**

833 We made cross-comparisons between ACOS V7.3 and other data sets. No bias was found in ACOS V7.3 from GEOS-Chem
834 with a standard deviation of 1.6 ppm and $R^2=0.77$. The comparison results in the cells are shown in Table 6. Generally,
835 ACOS V7.3 is in good agreement with all of them, which is reflected by correlation coefficients r that are above 0.85 and
836 greater than others, as shown in Table 6. The biggest differences up to 3.0 ppm for ACOS V7.3 are found from NIES and
837 OCFP in deserts cells, whereas differences from SRFP and EMMA are mostly within 1.0 ppm. This is similar to ACOS V3.5.
838 The total absolute difference from other algorithms (not including ACOS V3.5) is within 1.0 ppm in cells east of 110 °E but
839 above 2.0 ppm in cells west of 90 °E. It can also be found from Table 6 that the bias of ACOS V7.3 relative to GEOS-Chem
840 is within 0.3 ppm but above 1.3 ppm, in cells east and west of 90 °E, respectively.

841 Compared to the previous version, ACOS V3.5, ACOS V7.3 increases the average by approximately 0.2 ppm. In
 842 comparison with the difference patterns with ACOS V3.5, the averages of the absolute differences between ACOS V7.3 and
 843 the other four algorithms are similar (<0.1 ppm) and increase by an average of 0.6 ppm (2.1 ppm vs. 1.5 ppm) in cells east of
 844 110 °E and west of 90 °E, respectively, while the biases relative to GEOS-Chem decrease approximately 0.3 ppm and increase
 845 approximately 0.9 ppm in cells east and west of 90 °E, respectively.

846 The comparison results further demonstrate inconsistency of XCO₂ among different datasets in the desert cells.

847 ~~Table 6. Differences between ACOS V7.3 and others (including GEOS-Chem and five other algorithms including ACOS V3.5,~~
 848 ~~NIES, OCFP, SRFP and EMMA) in each cell (subtraction from ACOS V7.3). Values in parentheses are the corresponding~~
 849 ~~standard deviations.~~

Left longitude of cells(°E)	80	85	90	95	100	105	110	115	r
GEOS-Chem	-1.7(1.5) 64	-1.3(1.3) 85	0.1(1.2) 167	0.1(1.2) 191	-0.1(1.3) 294	0.3(1.6) 448	0(1.7) 487	0(1.6) 244	0.88
ACOS V3.5	-0.4(0.9) 103	-0.1(1.0) 48	-0.1(1.0) 133	-0.2(1.0) 189	0.0(1.1) 350	-0.5(1.1) 391	0.2(1.2) 244	-0.1(1.1) 126	0.93
NIES	-3.2(1.2) 61	-1.9(1.5) 100	-1.6(1.2) 251	-1.2(1.9) 123	-1.9(1.4) 541	-1.8(1.5) 317	-1.2(1.6) 397	-0.7(1.5) 277	0.87
OCFP	-3.1(1.0) 66	-3.4(0.9) 41	-2.2(1.1) 157	-2.5(1.5) 114	-2.1(1.2) 297	-1.5(1.1) 329	-0.5(1.1) 396	-0.1(1.0) 202	0.86
SRFP	-0.8(1.3) 138	-0.7(1.4) 145	0.3(1.3) 345	-0.6(1.3) 337	-0.4(1.3) 466	-0.5(1.4) 631	0.3(1.4) 447	0.1(1.2) 247	0.89
EMMA	-0.3(1.3) 113	-0.5(1.4) 90	0.0(1.0) 190	-0.4(1.4) 241	-0.2(1.3) 405	-0.3(1.2) 383	0.3(1.1) 390	0.5(1.1) 233	0.91
Average absolute difference [‡] for four algorithms above	2.2(1.1)	2.0(1.0)	1.4(0.7)	1.7(0.7)	1.6(0.6)	1.4(0.4)	1.1(0.3)	1.0(0.2)	

850 ~~‡ represents the average of absolute differences of ACOS V7.3 matching other algorithms including NIES, OCFP, SRFP and~~
 851 ~~EMMA for each cell.~~

852 6 Conclusion

853 Although TCCON has been widely accepted as the standard for validation of satellite-based XCO₂ data, it is necessary to
 854 better understand the performance of XCO₂ in spatial and timely variations at a regional scale and especially for those
 855 regions where ground-based measurements of XCO₂ are not available, such as for the TCCON stations in China. We
 856 implement the quantification and assessment of the agreement of multiple algorithms for typical regions with various land
 857 covers and enhancement of anthropogenic CO₂ emissions including the megacity of Beijing from 80 °E to 120 °E in the same
 858 latitude band of 40 °N to get better knowledge of the regional uncertainty and performance of GOSAT XCO₂ retrievals in
 859 China. Regional performance of XCO₂ products from four algorithms (ACOS, NIES, OCFP, SRFP) as well as GEOS-Chem

860 simulated XCO₂ are probed to obtain the regional uncertainty and attributions of GOSAT XCO₂ retrievals. In particular, we
 861 apply simulated XCO₂ at a high spatial resolution of 0.5 °(latitude) x 0.666 °(longitude) for a nested grid obtained by GEOS-
 862 Chem to assess the regional uncertainty of XCO₂ derived from satellite observations in China. In connection with the
 863 inconsistency of algorithms in eight cells, the characteristics of aerosol and albedo are investigated to discuss the further
 864 attribution of regional inconsistency of algorithms.

865 Summarizing the performance of four algorithms (ACOS, NIES, OCFP and SRFP) in each cell based on the above
 866 quantification and analysis from comparisons with GEOS-Chem, pairwise differences between algorithms and agreement in
 867 time series among algorithms, we can obtain the following results in general: (1)The consistency among algorithms is better
 868 in the east than in the west as the absolute difference from pairwise comparisons presents ~~0.9-1.5~~0.7-1.1 ppm in eastern cells
 869 covered by grassland, cropland and built-up areas with strong anthropogenic CO₂ emission whereas ~~1.2-2.2~~1.0-1.6 ppm in
 870 western cells covered by desert with a high-brightness surface with less anthropogenic CO₂ emission; (2) ACOS and SRFP
 871 are more satisfying in characterizing spatio-temporal patterns than other algorithms. To conclude, Table 10 presents the
 872 regional characteristics and a summary of the results described in above sections.

873 **Table 10. Summaries of our analyses for uncertainty of XCO₂ retrievals obtained by GOSAT via inter-comparison of multi-**
 874 **algorithms above, including characteristics of regional emissions, albedo, aerosol optical depth, and summary of differences**
 875 **between algorithms and bias compared to GEOS-Chem.**

<u>Characteristics of regions and summary of algorithms</u>		<u>Cells from 80 °E to 115 °E within 37°N-42°N</u>								
<u>Regions</u> <u>Left longitude (°E)</u>		<u>80</u>	<u>85</u>	<u>90</u>	<u>95</u>	<u>100</u>	<u>105</u>	<u>110</u>	<u>115</u>	
<u>Characteristics of regions</u>	<u>CO₂ emissions</u> <u>(Tg/year)*¹</u>	<u>Low emissions</u> <u>(1.2-57.1)</u>					<u>High emissions</u> <u>(515.2-821.9)</u>			
	<u>Property of aerosol</u> <u>(AOD)*²</u>	<u>Dust</u> <u>(0.22-0.53)</u>			<u>Clear</u> <u>(0.10-0.28)</u>			<u>Urban</u> <u>(0.10-0.37))</u>		
	<u>Surface types</u> <u>(albedo)</u>	<u>Sand desert with high</u> <u>brightness</u> <u>(0.20-0.26)</u>			<u>Gobi and grassland</u> <u>(0.19-0.22)</u>			<u>Cropland and</u> <u>built-up</u> <u>(0.14-0.17)</u>		
	<u>Consistency of algorithms</u> <u>(pairwise mean absolute</u> <u>differences)</u>	<u>Less Consistency</u> <u>(1.0-1.6 ppm)</u>					<u>Good consistency</u> <u>(0.7-1.1 ppm)</u>			
<u>Summary of uncertainty</u>	<u>Bias compared to</u> <u>GEOS-Chem</u> <u>(bias range)</u>	<u>Large biases</u> <u>(1.2-3.1 ppm)</u>					<u>lesser biases</u> <u>excluding NIES</u> <u>(0.0-0.5 ppm)</u>			
	<u>General performance of</u> <u>algorithms in spatio-</u> <u>temporal patterns of XCO₂</u> <u>compared to GEOS-Chem</u>	<u>ACOS presents the lowest bias (-0.1 ± 1.9 ppm);</u> <u>SRFP is next (-0.2 ± 2.2 ppm)</u> <u>NIES presents the greatest -2.0 ± 2.2 ppm)</u>								
<u>Left longitude of</u> <u>cells (°E)</u>	<u>80</u>	<u>85</u>	<u>90</u>	<u>95</u>	<u>100</u>	<u>105</u>	<u>110</u>	<u>115</u>		

876

CO ₂ emissions (Tg/year) ^{*1}	20.1 (24.1)	11.2 (7.8)	1.2 (2.7)	35.8 (20.7)	57.1 (15.6)	515.2 (199.0)	801.3 (600.3)	821.9 (893.3)		
Surface type	High brightness desert				Gobi desert					
Albedo	0.24	0.26	0.23	0.26	0.22	0.24	0.19	0.21	0.21	0.22
AOD ^{*2}	0.22	0.53	0.16	0.42	0.12	0.32	0.10	0.29	0.12	0.28
Regional Summary in pairwise differences between algorithms	Less Consistency (mean absolute differences 1.2-2.2 ppm) The difference of OCFP is the greatest with most of the other algorithms (1.7-2.2 ppm); next is NIES (1.6-2.2 ppm).						Good consistency (mean absolute differences 0.9-1.5 ppm) ACOS is relatively the least (0.9-1.1 ppm)			
Regional Summary compared to GEOS-Chem	Large biases, of which NIES is the greatest (1.4-3.1 ppm) and next is OCFP (1.2-2.2 ppm)						lesser biases (0.0-0.5 ppm) excluding NIES			
	Similar in seasonal amplitude;						Seasonal amplitude from GEOS-Chem is lower than all of satellite retrieval algorithms.			
Regional pairwise comparisons of ACOS v7.3	Greater biases are presented with OCFP (1.5-3.4 ppm) and NIES (1.2-3.2 ppm)						Lesser biases (0.0-0.5 ppm) excluding NIES			
General differences compared to GEOS-Chem	ACOS presents lowest values (bias -0.1 ppm Std ^{*3} 1.9 ppm), next is SRFP (bias -0.2 ppm Std 2.2 ppm) NIES presents the greatest (bias 2.0 ppm, Std 2.2 ppm).									
Spatio-temporal patterns of XCO ₂ compared to GEOS-Chem	ACOS and SRFP are similar to GEOS-Chem. OCFP is in better agreement with GEOS-Chem but the bias is larger.									

877 *¹ represents the total emissions of CO₂ from CHRED in each cell in 2012. *² is the range of averaged seasonal aerosol
878 optical depth over a year.

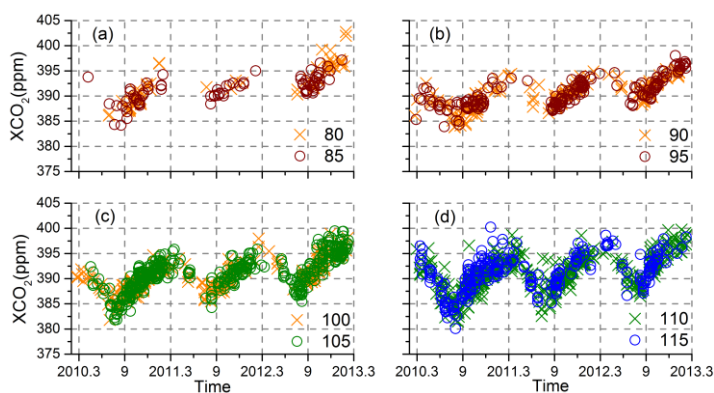
879

880 The results of our analysis, indicating that the discrepancies among algorithms are the smallest in eastern cells which
881 are the strongest anthropogenic emitting source regions in China, implies that the uncertainty of XCO₂ is likely low in this
882 area. It will be sufficiently rigorous for supporting us to apply GOSAT XCO₂ data in assessment of anthropogenic emissions
883 via timely changing magnitude of XCO₂ in such region. Moreover, it was likely that uncertainty in satellite-retrieved XCO₂
884 is attributed to the combined effects of aerosol and albedo. The large uncertainty of XCO₂ must be improved further, even
885 though many algorithms have endeavored to minimize the effects of aerosol and albedo. With the launch of OCO-2 in 2014
886 and GOSAT-2 scheduled for 2018, the prospect of a large amount of useful retrieved XCO₂ products is promising. Since low
887 regional XCO₂ biases are necessary for accurately estimating regional carbon sources and sinks, regional uncertainty should
888 be paid more attention in the future.

889 **Appendix A**

890 We made cross-comparisons between ACOS V7.3 and other data sets. The available data points of ACOS V7.3 were shown
 891 from March 2010 to February 2013 in Fig.S1. In cells west of 90 °E, there are a few data points showing abnormal
 892 concentrations as high as above 400.0 ppm, which is higher than that of data points in the east, where there are strong
 893 anthropogenic CO₂ emissions.

894 The comparison results in the cells are shown in Table S1. No bias was found in ACOS V7.3 from GEOS-Chem with a
 895 standard deviation of 1.6 ppm and R² of 0.77 in the whole study area. Generally, ACOS V7.3 is in good agreement with all
 896 of them, which is reflected by correlation coefficients r that are above 0.85 and greater than others, as shown in Table S1.
 897 The biggest differences up to 3.0 ppm for ACOS V7.3 are found from NIES and OCFP in deserts cells, whereas differences
 898 from SRFP are mostly within 1.0 ppm. This is similar to ACOS V3.5. The pairwise differences from other algorithms (not
 899 including ACOS V3.5) are up to 1.9 ppm in cells west of 90 °E, which is distinctly high, whereas within 0.9 ppm in cells east
 900 of 110 °E. It can also be found that the bias of ACOS V7.3 relative to GEOS-Chem is within 0.3 ppm but above 1.3 ppm, in
 901 cells east and west of 90 °E, respectively.



902
 903 **Fig. S1. The time series of data points from ACOS V7.3 during the period from March 2010 to February 2013. Different symbols**
 904 **in each panel represent the left longitude of the cell into which a data point falls.**

905 **Table S1. Differences between ACOS V7.3 and others (including GEOS-Chem and four other algorithms including ACOS V3.5,**
 906 **NIES, OCFP and SRFP) in each cell (subtraction from ACOS V7.3). Values in parentheses are the corresponding standard**
 907 **deviations.**

<u>Left longitude of cells(°E)</u>	<u>80</u>	<u>85</u>	<u>90</u>	<u>95</u>	<u>100</u>	<u>105</u>	<u>110</u>	<u>115</u>	<u>r</u>
<u>GEOS-Chem</u>	<u>-1.7(1.5)</u> 64	<u>-1.3(1.3)</u> 85	<u>0.1(1.2)</u> 167	<u>0.1(1.2)</u> 191	<u>-0.1(1.3)</u> 294	<u>0.3(1.6)</u> 448	<u>0(1.7)</u> 487	<u>0(1.6)</u> 244	<u>0.88</u>
<u>ACOS V3.5</u>	<u>-0.4(0.9)</u> 103	<u>-0.1(1.0)</u> 48	<u>-0.1(1.0)</u> 133	<u>-0.2(1.0)</u> 189	<u>0.0(1.1)</u> 350	<u>-0.5(1.1)</u> 391	<u>0.2(1.2)</u> 244	<u>-0.1(1.1)</u> 126	<u>0.93</u>
<u>NIES</u>	<u>-3.2(1.2)</u> 61	<u>-1.9(1.5)</u> 100	<u>-1.6(1.2)</u> 251	<u>-1.2(1.9)</u> 123	<u>-1.9(1.4)</u> 541	<u>-1.8(1.5)</u> 317	<u>-1.2(1.6)</u> 397	<u>-0.7(1.5)</u> 277	<u>0.87</u>
<u>OCFP</u>	<u>-3.1(1.0)</u>	<u>-3.4(0.9)</u>	<u>-2.2(1.1)</u>	<u>-2.5(1.5)</u>	<u>-2.1(1.2)</u>	<u>-1.5(1.1)</u>	<u>-0.5(1.1)</u>	<u>-0.1(1.0)</u>	<u>0.86</u>

	<u>66</u>	<u>41</u>	<u>157</u>	<u>114</u>	<u>297</u>	<u>329</u>	<u>396</u>	<u>202</u>	
<u>SRFP</u>	<u>-0.8(1.3)</u>	<u>-0.7(1.4)</u>	<u>0.3(1.3)</u>	<u>-0.6(1.3)</u>	<u>-0.4(1.3)</u>	<u>-0.5(1.4)</u>	<u>0.3(1.4)</u>	<u>0.1(1.2)</u>	<u>0.89</u>
	<u>138</u>	<u>145</u>	<u>345</u>	<u>337</u>	<u>466</u>	<u>631</u>	<u>447</u>	<u>247</u>	
<u>Average absolute difference¹ for three algorithms above</u>	<u>1.9(1.5)</u>	<u>1.7(1.4)</u>	<u>1.2(1.0)</u>	<u>1.4(1.1)</u>	<u>1.3(1.0)</u>	<u>1.2(0.8)</u>	<u>0.9(0.7)</u>	<u>0.7(0.5)</u>	

908 *¹ represents the average of absolute differences of ACOS V7.3 matching other algorithms including NIES, OCFP and SRFP for
909 each cell.

910

911

912 Acknowledgements: This research was supported by the National Research Program on Global Changes and Adaptation:
913 “Big data on global changes: data sharing platform and recognition” (Grant No. 2016YFA0600303, 2016YFA0600304). We
914 are grateful for NIES products from NIES GOSAT Project, albedo data from Beijing Normal University, XCO₂ data from
915 the TCCON data archive, operated by the California Institute of Technology, and supports from GEOS-Chem team. ACOS
916 V3.5 and ACOS V7.3 were produced by the ACOS/OCO-2 project at the Jet Propulsion Laboratory, California Institute of
917 Technology, and obtained from the JPL website, <http://CO2.jpl.nasa.gov> . We are grateful for aerosol data from Aeronautics
918 and Space Administration (NASA). The satellite XCO₂ products OCFP and SRFP have been obtained from the ESA project
919 GHG-CCI website (<http://www.esa-ghg-cci.org/>) and the data providers Univ. Leicester (OCFP product) and SRON & KIT
920 (SRFP) have granted permission to use these data for peer-reviewed publications.

921 **References**

922 Andres, R. J., Boden, T. A., Br on, F. M., Ciais, P., Davis, S., Erickson, D., Gregg, J. S., Jacobson, A., Marland, G., Miller,
923 J., Oda, T., Olivier, J. G. J., Raupach, M. R., Rayner, P., and Treanton, K.: A synthesis of carbon dioxide emissions from
924 fossil-fuel combustion, Biogeosciences, 9, 1845-1871, <https://doi.org/10.5194/bg-9-1845-2012>, 2012.

925 Bie, N., Lei, L., He, Z., and Liu, M.: An analysis of atmospheric CO₂ concentration around the takelamagan desert with five
926 products retrieved from satellite observations, International Geoscience and Remote Sensing Symposium (IGARSS), Beijing,
927 China, 10-15 July 2016, <https://doi.org/10.1109/IGARSS.2016.7730064>, 2016.

928 Blumenstock, T., Hase, F., Schneider, M., Garcia, O. E. and Sepulveda, E.: TCCON data from Izana, Tenerife, Spain,
929 Release GGG2014R0, TCCON data archive, CDIAC, <https://doi.org/10.14291/tcon.ggg2014.izana01.R0/1149295>, 2014.

930 Bovensmann, H., Burrows, J. P., Buchwitz, M., Frerick, J., No , S., Rozanov, V. V., Chance, K. V., and Goede, A. P. H.:
931 SCIAMACHY: Mission Objectives and Measurement Modes, J. Atmos. Sci., 56, 127-150, 1999.

932 Buchwitz, M., Reuter, M., Schneising, O., Boesch, H., Guerlet, S., Dils, B., Aben, I., Armante, R., Bergamaschi, P.,
933 Blumenstock, T., Bovensmann, H., Brunner, D., Buchmann, B., Burrows, J. P., Butz, A., Ch din, A., Chevallier, F.,

934 Crevoisier, C. D., Deutscher, N. M., Frankenberg, C., Hase, F., Hasekamp, O. P., Heymann, J., Kaminski, T., Laeng, A.,
935 Lichtenberg, G., De Mazière, M., Nođ, S., Notholt, J., Orphal, J., Popp, C., Parker, R., Scholze, M., Sussmann, R., Stiller, G.
936 P., Warneke, T., Zehner, C., Bril, A., Crisp, D., Griffith, D. W. T., Kuze, A., O'Dell, C., Oshchepkov, S., Sherlock, V., Suto,
937 H., Wennberg, P., Wunch, D., Yokota, T., and Yoshida, Y.: The Greenhouse Gas Climate Change Initiative (GHG-CCI):
938 Comparison and quality assessment of near-surface-sensitive satellite-derived CO₂ and CH₄ global data sets, *Remote Sens.*
939 *Environ.*, 162, 344-362, <http://dx.doi.org/10.1016/j.rse.2013.04.024> , 2015.

940 Burrows, J. P., Hölzle, E., Goede, A. P. H., Visser, H., and Fricke, W.: SCIAMACHY—scanning imaging absorption
941 spectrometer for atmospheric cartography, *Acta Astronaut.*, 35, 445-451, [https://doi.org/10.1016/0094-5765\(94\)00278-T](https://doi.org/10.1016/0094-5765(94)00278-T) ,
942 1995.

943 Butz, A., Guerlet, S., Hasekamp, O., Schepers, D., Galli, A., Aben, I., Frankenberg, C., Hartmann, J. M., Tran, H., Kuze, A.,
944 Keppel-Aleks, G., Toon, G., Wunch, D., Wennberg, P., Deutscher, N., Griffith, D., Macatangay, R., Messerschmidt, J.,
945 Notholt, J., and Warneke, T.: Toward accurate CO₂ and CH₄ observations from GOSAT, *Geophys. Res. Lett.*, 38, n/a-n/a,
946 <https://doi.org/10.1029/2011gl047888> , 2011.

947 Cai, B., and Zhang, L.: Urban CO₂ emissions in China: Spatial boundary and performance comparison, *Energy Policy*, 66,
948 557-567, <https://doi.org/10.1016/j.enpol.2013.10.072> , 2014.

949 Chen, B.: Seasonal migration of cirrus clouds over the Asian Monsoon regions and the Tibetan Plateau measured from
950 MODIS/Terra, *Geophys. Res. Lett.*, 32, <https://doi.org/10.1029/2004gl020868>, 2005.

951 Ciaï, P., Rayner, P., Chevallier, F., Bousquet, P., Logan, M., Peylin, P., and Ramonet, M.: Atmospheric inversions for
952 estimating CO₂ fluxes: methods and perspectives, *Climatic Change*, 103, 69-92, <https://doi.org/10.1007/s10584-010-9909-3>,
953 2010.

954 Cogan, A. J., Boesch, H., Parker, R. J., Feng, L., Palmer, P. I., Blavier, J. F. L., Deutscher, N. M., Macatangay, R., Notholt,
955 J., Roehl, C., Warneke, T., and Wunch, D.: Atmospheric carbon dioxide retrieved from the Greenhouse gases Observing
956 SATellite (GOSAT): Comparison with ground-based TCCON observations and GEOS-Chem model calculations, *J.*
957 *Geophys. Res. Atmos.*, 117, n/a-n/a, <https://doi.org/10.1029/2012jd018087>, 2012.

958 Connor, B. J., Boesch, H., Toon, G., Sen, B., Miller, C., and Crisp, D.: Orbiting Carbon Observatory: Inverse method and
959 prospective error analysis, *J. Geophys. Res. Atmos.*, 113, n/a-n/a, <https://doi.org/10.1029/2006jd008336>, 2008.

960 Detmers, R., Hasekamp, O.: Product User Guide (PUG) for the RemoTeC XCO₂ Full Physics GOSAT Data Product,
961 available at http://www.esa-ghg-cci.org/sites/default/files/documents/public/documents/GHG-CCI_DATA.html, 2015.

962 Deutscher, N., Notholt, J., Messerschmidt, J., Weinzierl, C., Warneke, T., Petri, C., Grupe, P. and Katrynski, K.: TCCON
963 data from Bialystok, Poland, Release GGG2014R1, TCCON data archive, CDIAC,
964 <https://doi.org/10.14291/tccon.ggg2014.bialystok01.R1/1183984>, 2014.

965 GHG-CCI group at University of Leicester: Algorithm Theoretical Basis Document Version 3 (ATBDv3)-The University of
966 Leicester Full-Physics Retrieval Algorithm for the retrieval of XCO₂ and XCH₄, available at http://www.esa-ghg-cci.org/sites/default/files/documents/public/documents/GHG-CCI_DATA.html, 2014.

967

968 Giglio, L., Randerson, J. T., and van der Werf, G. R.: Analysis of daily, monthly, and annual burned area using the fourth-
969 generation global fire emissions database (GFED4), *J. Geophys. Res. Biogeosci.*, 118, 317-328,
970 <https://doi.org/10.1002/jgrg.20042>, 2013.

971 Graven, H. D., Keeling, R. F., Piper, S. C., Patra, P. K., Stephens, B. B., Wofsy, S. C., Welp, L. R., Sweeney, C., Tans, P. P.,
972 Kelley, J. J., Daube, B. C., Kort, E. A., Santoni, G. W., and Bent, J. D.: Enhanced seasonal exchange of CO₂ by northern
973 ecosystems since 1960, *Science*, 341, 1085-1089, <https://doi.org/10.1126/science.1239207>, 2013.

974 Griffith, D. W. T., Deutscher, N., Velazco, V. A., Wennberg, P. O., Yavin, Y., Aleks, G. K., Washenfelder, R., Toon, G. C.,
975 Blavier, J. F., Murphy, C., Jones, N., Kettlewell, G., Connor, B., Macatangay, R., Roehl, C., Ryzcek, M., Glowacki, J.,
976 Culgan, T. and Bryant, G.: TCCON data from Darwin, Australia, Release GGG2014R0, TCCON data archive, CDIAC,
977 <https://doi.org/10.14291/tcon.ggg2014.darwin01.R0/1149290>, 2014a.

978 Griffith, D. W. T., Velazco, V. A., Deutscher, N., Murphy, C., Jones, N., Wilson, S., Macatangay, R., Kettlewell, G.,
979 Buchholz, R. R. and Riggenschach, M.: TCCON data from Wollongong, Australia, Release GGG2014R0, TCCON data
980 archive, CDIAC, <https://doi.org/10.14291/tcon.ggg2014.wollongong01.R0/1149291>, 2014b.

981 Goddard Earth Science Data Information and Services Center: ACOS Level 2 Standard Product Data User's Guide, v3.5,
982 available at <http://co2.jpl.nasa.gov>, 2016.

983 Goddard Earth Science Data Information and Services Center: ACOS Level 2 Standard Product Data User's Guide, v7.3,
984 available at <http://co2.jpl.nasa.gov>, 2017.

985 Guan, D., Liu, Z., Geng, Y., Lindner, S., and Hubacek, K.: The gigatonne gap in China's carbon dioxide inventories, *Nature*
986 *Clim. Change*, 2, 672-675, <https://doi.org/10.1038/nclimate1560>, 2012.

987 Guerlet, S., Butz, A., Schepers, D., Basu, S., Hasekamp, O. P., Kuze, A., Yokota, T., Blavier, J. F., Deutscher, N. M.,
988 Griffith, D. W. T., Hase, F., Kyro, E., Morino, I., Sherlock, V., Sussmann, R., Galli, A., and Aben, I.: Impact of aerosol and
989 thin cirrus on retrieving and validating XCO₂ from GOSAT shortwave infrared measurements, *J. Geophys. Res. Atmos.*, 118,
990 4887-4905, <https://doi.org/10.1002/jgrd.50332>, 2013.

991 Hase, F., Blumenstock, T., Dohe, S., Gross, J. and Kiel, M.: TCCON data from Karlsruhe, Germany, Release GGG2014R1,
992 TCCON data archive, CDIAC, <https://doi.org/10.14291/tcon.ggg2014.karlsruhe01.R1/1182416>, 2014.

993 Hasekamp, O., Hu, H., Detmers, R., and Butz, A.: ESA Climate Change Initiative (CCI) Algorithm Theoretical Basis
994 Document for the RemoTeC XCO₂ and XCH₄ Full Physics Products of the Essential Climate Variable (ECV) Greenhouse

995 Gases (GHG), available at <http://www.esa-ghg-cci.org/sites/default/files/documents/public/documents/GHG->
996 [CCI_DATA.html](http://www.esa-ghg-cci.org/sites/default/files/documents/public/documents/GHG-CCI_DATA.html), 2015.

997 He, Z., Zeng, Z.-C., Lei, L., Bie, N., and Yang, S.: A Data-Driven Assessment of Biosphere-Atmosphere Interaction Impact
998 on Seasonal Cycle Patterns of XCO₂ Using GOSAT and MODIS Observations, *Remote Sens.*, 9, 251,
999 <https://doi.org/10.3390/rs9030251>, 2017.

1000 Hewson, W.: Product User Guide:University of Leicester full-physics XCO₂ retrieval algorithm for CRDP3 – OCFP v6.0,
1001 available at http://www.esa-ghg-cci.org/sites/default/files/documents/public/documents/GHG-CCI_DATA.html, 2016.

1002 Kawakami, S., Ohyama, H., Arai, K., Okumura, H., Taura, C., Fukamachi, T. and Sakashita, M.: TCCON data from Saga,
1003 Japan, Release GGG2014R0, TCCON data archive, CDIAC, <https://doi.org/10.14291/tcon.ggg2014.saga01.R0/1149283>,
1004 2014.

1005 Keeling, C. D., Bacastow, R. B., Bainbridge, A. E., Ekdahl Jr., C. A., Guenther, P. R., Waterman, L. S., and Chin, J. F. S.:
1006 Atmospheric carbon dioxide variations at Mauna Loa Observatory, Hawaii, *Tellus A*, 28,
1007 <https://doi.org/10.3402/tellusa.v28i6.11322>, 2011.

1008 Keller, C. A., Long, M. S., Yantosca, R. M., Da Silva, A. M., Pawson, S., and Jacob, D. J.: HEMCO v1.0: a versatile,
1009 ESMF-compliant component for calculating emissions in atmospheric models, *Geosci. Model Dev.*, 7, 1409-1417,
1010 <https://doi.org/10.5194/gmd-7-1409-2014>, 2014.

1011 Keppel-Aleks, G., Wennberg, P. O., O'Dell, C. W., and Wunch, D.: Towards constraints on fossil fuel emissions from total
1012 column carbon dioxide, *Atmos. Chem. Phys.*, 13, 4349-4357, <https://doi.org/10.5194/acp-13-4349-2013>, 2013.

1013 Kivi, R., Heikkinen, P. and Kyro, E.: TCCON data from Sodankyla, Finland, Release GGG2014R0, TCCON data archive,
1014 CDIAC, <https://doi.org/10.14291/tcon.ggg2014.sodankyla01.R0/1149280>, 2014.

1015 Kulawik, S., Wunch, D., Aros, Dell, C., Frankenberg, C., Reuter, M., Oda, T., Chevallier, F., Sherlock, V., Buchwitz, M.,
1016 Osterman, G., Miller, C. E., Wennberg, P. O., Griffith, D., Morino, I., Dubey, M. K., Deutscher, N. M., Notholt, J., Hase, F.,
1017 Warneke, T., Sussmann, R., Robinson, J., Strong, K., Schneider, M., De Mazière, M., Shiomi, K., Feist, D. G., Iraci, L. T.,
1018 and Wolf, J.: Consistent evaluation of ACOS-GOSAT, BESD-SCIAMACHY, CarbonTracker, and MACC through
1019 comparisons to TCCON, *Atmos. Meas. Tech.*, 9, 683-709, <https://doi.org/10.5194/amt-9-683-2016>, 2016.

1020 Lei, H., and Yang, D.: Seasonal and interannual variations in carbon dioxide exchange over a cropland in the North China
1021 Plain, *Glob. Chang. Biol.*, 16, 2944-2957, <https://doi.org/10.1111/j.1365-2486.2009.02136.x>, 2010.

1022 Lei, L., Guan, X., Zeng, Z., Zhang, B., Ru, F., and Bu, R.: A comparison of atmospheric CO₂ concentration GOSAT-based
1023 observations and model simulations, *Sci. Chin.-Earth Sci.*, 57, 1393-1402, <https://doi.org/10.1007/s11430-013-4807-y>, 2014.

1024 Lindqvist, H., O'Dell, C. W., Basu, S., Boesch, H., Chevallier, F., Deutscher, N., Feng, L., Fisher, B., Hase, F., Inoue, M.,
1025 Kivi, R., Morino, I., Palmer, P. I., Parker, R., Schneider, M., Sussmann, R., and Yoshida, Y.: Does GOSAT capture the true
1026 seasonal cycle of carbon dioxide?, *Atmos. Chem. Phys.*, 15, 13023-13040, <https://doi.org/10.5194/acp-15-13023-2015>, 2015.

1027 Liu, D., Lei, L., Guo, L., and Zeng, Z.-C.: A Cluster of CO₂ Change Characteristics with GOSAT Observations for Viewing
1028 the Spatial Pattern of CO₂ Emission and Absorption, *Atmosphere*, 6, 1695-1713, <https://doi.org/10.3390/atmos6111695>,
1029 2015.

1030 Liu, Z., Guan, D., Wei, W., Davis, S. J., Ciais, P., Bai, J., Peng, S., Zhang, Q., Hubacek, K., Marland, G., Andres, R. J.,
1031 Crawford-Brown, D., Lin, J., Zhao, H., Hong, C., Boden, T. A., Feng, K., Peters, G. P., Xi, F., Liu, J., Li, Y., Zhao, Y., Zeng,
1032 N., and He, K.: Reduced carbon emission estimates from fossil fuel combustion and cement production in China, *Nature*,
1033 524, 335-338, <https://doi.org/10.1038/nature14677>, 2015.

1034 Messerschmidt, J., Parazoo, N., Wunch, D., Deutscher, N. M., Roehl, C., Warneke, T., and Wennberg, P. O.: Evaluation of
1035 seasonal atmosphere–biosphere exchange estimations with TCCON measurements, *Atmos. Chem. Phys.*, 13, 5103-5115,
1036 <https://doi.org/10.5194/acp-13-5103-2013>, 2013.

1037 Morino, I., Matsuzaki, T. and Shishime, A.: TCCON data from Tsukuba, Ibaraki, Japan, 125HR, Release GGG2014R1,
1038 TCCON data archive, CDIAC, <https://doi.org/10.14291/tcon.ggg2014.tsukuba02.R1/1241486>, 2014.

1039 Nassar, R., Jones, D. B. A., Suntharalingam, P., Chen, J. M., Andres, R. J., Wecht, K. J., Yantosca, R. M., Kulawik, S. S.,
1040 Bowman, K. W., Worden, J. R., Machida, T., and Matsueda, H.: Modeling global atmospheric CO₂ with improved emission
1041 inventories and CO₂ production from the oxidation of other carbon species, *Geosci. Model Dev.*, 3, 689-716,
1042 <https://doi.org/10.5194/gmd-3-689-2010>, 2010.

1043 Nassar, R., Napier-Linton, L., Gurney, K. R., Andres, R. J., Oda, T., Vogel, F. R., and Deng, F.: Improving the temporal and
1044 spatial distribution of CO₂ emissions from global fossil fuel emission data sets, *J. Geophys. Res. Atmos.*, 118, 917-933,
1045 <https://doi.org/10.1029/2012jd018196>, 2013.

1046 National Institute for Environmental Studies, GOSAT Project Office: NIES GOSAT TANSO-FTS SWIR Level 2 Data
1047 Product Format Description Version 2.50, available at <https://data2.gosat.nies.go.jp/doc/document.html#Document>, 2015.

1048 Oda, T., and Maksyutov, S.: A very high-resolution (1 km×1 km) global fossil fuel CO₂ emission inventory derived using a
1049 point source database and satellite observations of nighttime lights, *Atmos. Chem. Phys.*, 11, 543-556,
1050 <https://doi.org/10.5194/acp-11-543-2011>, 2011.

1051 O'Dell, C. W., Connor, B., Bösch, H., O'Brien, D., Frankenberg, C., Castano, R., Christi, M., Eldering, D., Fisher, B.,
1052 Gunson, M., McDuffie, J., Miller, C. E., Natraj, V., Oyafuso, F., Polonsky, I., Smyth, M., Taylor, T., Toon, G. C., Wennberg,
1053 P. O., and Wunch, D.: The ACOS CO₂ retrieval algorithm – Part 1: Description and validation against synthetic observations,
1054 *Atmos. Meas. Tech.*, 5, 99-121, <https://doi.org/10.5194/amt-5-99-2012>, 2012.

1055 Oshchepkov, S., Bril, A., Yokota, T., Wennberg, P. O., Deutscher, N. M., Wunch, D., Toon, G. C., Yoshida, Y., O'Dell, C.
1056 W., Crisp, D., Miller, C. E., Frankenberg, C., Butz, A., Aben, I., Guerlet, S., Hasekamp, O., Boesch, H., Cogan, A., Parker,
1057 R., Griffith, D., Macatangay, R., Notholt, J., Sussmann, R., Rettinger, M., Sherlock, V., Robinson, J., Kyrö, E., Heikkinen, P.,
1058 Feist, D. G., Morino, I., Kadyrov, N., Belikov, D., Maksyutov, S., Matsunaga, T., Uchino, O., and Watanabe, H.: Effects of
1059 atmospheric light scattering on spectroscopic observations of greenhouse gases from space. Part 2: Algorithm
1060 intercomparison in the GOSAT data processing for CO₂ retrievals over TCCON sites, *J. Geophys. Res. Atmos.*, 118, 1493-
1061 1512, <https://doi.org/10.1002/jgrd.50146>, 2013.

1062 Sherlock, V., Connor, B., Robinson, J., Shiona, H., Smale, D. and Pollard, D.: TCCON data from Lauder, New Zealand,
1063 125HR, Release GGG2014R0, TCCON data archive, CDIAC, <https://doi.org/10.14291/tcon.ggg2014.lauder02.R0/1149298>,
1064 2014.

1065 Sussmann, R. and Rettinger, M.: TCCON data from Garmisch, Germany, Release GGG2014R0, TCCON data archive,
1066 CDIAC, <https://doi.org/10.14291/tcon.ggg2014.garmisch01.R0/1149299>, 2014.

1067 Takahashi, T., Sutherland, S. C., Wanninkhof, R., Sweeney, C., Feely, R. A., Chipman, D. W., Hales, B., Friederich, G.,
1068 Chavez, F., and Sabine, C.: Takahashi, T. et al. Climatological mean and decadal changes in surface ocean pCO₂, and net
1069 sea-air CO₂ flux over the global oceans, *Deep-Sea Res. Pt. II*, 56, 554-577, <https://doi.org/10.1016/j.dsr2.2008.12.009>, 2009.

1070 Thoning, K. W., Tans, P. P., and Komhyr, W. D.: Atmospheric carbon dioxide at Mauna Loa Observatory: 2. Analysis of the
1071 NOAA GMCC data, 1974-1985, *J. Geophys. Res. Atmos.*, 94, 8549-8565, <https://doi.org/10.1029/JD094iD06p08549>, 1989.

1072 Wang, J., Cai, B., Zhang, L., Cao, D., Liu, L., Zhou, Y., Zhang, Z., and Xue, W.: High resolution carbon dioxide emission
1073 gridded data for China derived from point sources, *Environ. Sci. Technol.*, 48, 7085-7093, <https://doi.org/10.1021/es405369r>,
1074 2014.

1075 Wang, W., Tian, Y., Liu, C., Sun, Y., Liu, W., Xie, P., Liu, J., Xu, J., Morino, I., Velasco, V. A., Griffith, D. W. T., Notholt,
1076 J., and Warneke, T.: Investigating the performance of a greenhouse gas observatory in Hefei, China, *Atmos. Meas. Tech.*, 10,
1077 2627-2643, <https://doi.org/10.5194/amt-10-2627-2017>, 2017..

1078 Wang Min-zhong, H. Q., Wei Wen-shou, Yang Lian-mei, and Zhao Yong: Observational Analysis of the Troposphere and
1079 Low Stratosphere at Minfeng Station in the North Side of the Tibetan Plateau in July 2011, *Plateau Meteorology*, 31, 12,
1080 2012.

1081 Warneke, T., Messerschmidt, J., Notholt, J., Weinzierl, C., Deutscher, N., Petri, C., Grupe, P., Vuillemin, C., Truong, F.,
1082 Schmidt, M., Ramonet, M. and Parmentier, E.: TCCON data from Orleans, France, Release GGG2014R0, TCCON data
1083 archive, CDIAC, <https://doi.org/10.14291/tcon.ggg2014.orleans01.R0/1149276>, 2014.

1084 Watson, D. F., and Philip, G. M.: Triangle based interpolation, *Mathematical Geology*, 16, 779-795,
1085 <https://doi.org/10.1007/BF01036704>, 1984.

1086 Wennberg, P. O., Roehl, C., Blavier, J. F., Wunch, D., Landeros, J. and Allen, N.: TCCON data from Jet Propulsion
1087 Laboratory, Pasadena, California, USA, Release GGG2014R0, TCCON data archive, CDIAC,
1088 <https://doi.org/10.14291/tccon.ggg2014.jpl02.R0/1149297>, 2014a.

1089 Wennberg, P. O., Roehl, C., Wunch, D., Toon, G. C., Blavier, J. F., Washenfelder, R., Keppel-Aleks, G., Allen, N. and
1090 Ayers, J.: TCCON data from Park Falls, Wisconsin, USA, Release GGG2014R0, TCCON data archive, CDIAC,
1091 <https://doi.org/10.14291/tccon.ggg2014.parkfalls01.R0/1149161>, 2014b.

1092 Wennberg, P. O., Wunch, D., Roehl, C., Blavier, J. F., Toon, G. C., Allen, N., Dowell, P., Teske, K., Martin, C. and Martin,
1093 J.: TCCON data from Lamont, Oklahoma, USA, Release GGG2014R0, TCCON data archive, CDIAC,
1094 <https://doi.org/10.14291/tccon.ggg2014.lamont01.R0/1149159>, 2014c.

1095 Wunch, D., Wennberg, P. O., Toon, G. C., Connor, B. J., Fisher, B., Osterman, G. B., Frankenberg, C., Mandrake, L., O'Dell,
1096 C., Ahonen, P., Biraud, S. C., Castano, R., Cressie, N., Crisp, D., Deutscher, N. M., Eldering, A., Fisher, M. L., Griffith, D.
1097 W. T., Gunson, M., Heikkinen, P., Keppel-Aleks, G., Kyr ö E., Lindenmaier, R., Macatangay, R., Mendonca, J.,
1098 Messerschmidt, J., Miller, C. E., Morino, I., Notholt, J., Oyafuso, F. A., Rettinger, M., Robinson, J., Roehl, C. M., Salawitch,
1099 R. J., Sherlock, V., Strong, K., Sussmann, R., Tanaka, T., Thompson, D. R., Uchino, O., Warneke, T., and Wofsy, S. C.: A
1100 method for evaluating bias in global measurements of CO₂ total columns from space, *Atmos. Chem. Phys.*, 11, 12317-12337,
1101 <https://doi.org/10.5194/acp-11-12317-2011>, 2011.

1102 Yokota, T., Oguma, H., Morino, I., and Inoue, G.: A nadir looking SWIR sensor to monitor CO₂ column density for
1103 Japanese GOSAT project, Proceedings of the twenty-fourth international symposium on space technology and science,
1104 Miyazaki: Japan Society for Aeronautical and Space Sciences and ISTS, 887-889, 2004.

1105 Yoshida, Y., Kikuchi, N., Morino, I., Uchino, O., Oshchepkov, S., Bril, A., Saeki, T., Schutgens, N., Toon, G. C., Wunch, D.,
1106 Roehl, C. M., Wennberg, P. O., Griffith, D. W. T., Deutscher, N. M., Warneke, T., Notholt, J., Robinson, J., Sherlock, V.,
1107 Connor, B., Rettinger, M., Sussmann, R., Ahonen, P., Heikkinen, P., Kyr ö E., Mendonca, J., Strong, K., Hase, F., Dohe, S.,
1108 and Yokota, T.: Improvement of the retrieval algorithm for GOSAT SWIR XCO₂ and XCH₄ and their validation using
1109 TCCON data, *Atmos. Meas. Tech.*, 6, 1533-1547, <https://doi.org/10.5194/amt-6-1533-2013>, 2013.

1110 Zeng, Z.-C., Lei, L., Strong, K., Jones, D. B. A., Guo, L., Liu, M., Deng, F., Deutscher, N. M., Dubey, M. K., Griffith, D. W.
1111 T., Hase, F., Henderson, B., Kivi, R., Lindenmaier, R., Morino, I., Notholt, J., Ohyama, H., Petri, C., Sussmann, R., Velazco,
1112 V. A., Wennberg, P. O., and Lin, H.: Global land mapping of satellite-observed CO₂ total columns using spatio-temporal
1113 geostatistics, *Int. J. Digit. Earth*, 1-31, <https://doi.org/10.1080/17538947.2016.1156777>, 2016.

1114 Zhang, X. Y., Wang, Y. Q., Niu, T., Zhang, X. C., Gong, S. L., Zhang, Y. M., and Sun, J. Y.: Atmospheric aerosol
1115 compositions in China: spatial/temporal variability, chemical signature, regional haze distribution and comparisons with
1116 global aerosols, *Atmos. Chem. Phys.*, 12, 779-799, <https://doi.org/10.5194/acp-12-779-2012>, 2012.